Inorg. Chem. **2007**, *46*, 9067–9082

Inorganic Chemistry Article

Hydrothermal Synthesis, Structural Chemistry, and Magnetic Properties of Materials of the M^{II}/Triazolate/Anion Family, Where M^{II} = Mn, Fe, and Ni

Wayne Ouellette,[†] **Andrey V. Prosvirin,**[‡] **Jamie Valeich,**[†] **Kim R. Dunbar,**[‡] **and Jon Zubieta***[,†]

Department of Chemistry, Syracuse University, Syracuse, New York 13244, and
Department of Chemistry, Texas A&M University, College Station, Texas 77842

Received April 25, 2007

Hydrothermal chemistry has been exploited in the preparation of a series of manganese(II), iron(II), and nickel(II) triazolate frameworks, $[Mn_7(trz)_8(CH_3CO_2)_4(OH)_2]\cdot 2.5H_2O$ ($\mathbf{1}\cdot 2.5H_2O$), $[Mn_5(Htrz)_2(SO_4)_4(OH)_2]$ (**2**), $[Fe_5(Htrz)_2(SO_4)_4(OH)_2]$ (**3**), $[Fe_3(Htrz)_3(HSO_4)(SO_4)_2(OH)]\cdot H_2O$ ($\mathbf{4}\cdot H_2O$), $[Ni_3(trz)_3(OH)_3(H_2O)_4]\cdot 5H_2O$ ($\mathbf{5}\cdot 5H_2O$), and $[Ni_3(trz)_5(OH)]\cdot 2.5H_2O$ ($\mathbf{6}\cdot 2.5H_2O$). The materials all exhibit three-dimensional structures, reflecting the tendency of triazole/triazolate ligands to bridge multiple metal sites. A prominent characteristic of the structures is the presence of embedded metal clusters as building blocks: heptanuclear Mn^{II} units in **1**, pentanuclear M^{II} sites in **2** and **3**, and trinuclear M^{II} clusters in **4** and **5**. The presence of the pentanuclear and trinuclear clusters of magnetic metal cations in **2**–**5** is reflected in the unusual magnetic characteristics of these materials, all of which exhibit spin frustration. The compound $\mathbf{5}\cdot 5H_2O$ reversibly desorbs/sorbs solvent. However, the dehydrated phase does not adsorb methanol, N_2, O_2, or H_2, presumably as a consequence of the highly polar void volume and the narrow channels connecting the larger cavities of the void structure.

Introduction

The significant contemporary interest in organic–inorganic hybrid materials reflects both the fundamental chemistry of the rational design of complex materials and practical applications to fields as diverse as catalysis,[1] optical materials,[2,3] membranes,[4–6] and sorption.[7–9] Such materials combine the unique features of the organic and inorganic components in a complementary fashion, giving rise to diverse structural chemistry and composite or novel physical properties and providing access to a vast domain of complex, multifunctional materials.

Prototypical organic–inorganic hybrids include materials constructed from metal or metal cluster nodes linked through polyfunctional carboxylates, polypyridyl ligands, and organodiphosphonate ligands.[10–22] More recently, polyazahet-

---

* To whom correspondence should be addressed. E-mail: jazubiet@syr.edu. Fax: 315-443-4070.

[†] Syracuse University.

[‡] Texas A&M University.

(1) For example, see: (a) Ngo, H. L.; Hu, A. G.; Lin, W. B. *J. Mol. Catal. A* **2004**, *215*, 177. (b) Evans, O. R.; Ngo, H. L.; Lin, W. B. *J. Am. Chem. Soc.* **2001**, *123*, 10395. (c) Vioux, A.; Le Bideau, J.; Mutin, P. H.; Leclercq, D. *New Aspects in Phosphorus Chemistry IV*; Springer: New York, 2004; Vol. 232, pp 145–174.

(2) Sanchez, C.; Lebeau, B.; Chaput, F.; Boilet, J. P. *Adv. Mater.* **2003**, *15*, 1969.

(3) Evans, O. R.; Lin, W. B. *Chem. Mater.* **2001**, *13*, 3009.

(4) Jannasch, P. *Curr. Opin. Colloid Interface Sci.* **2003**, *8*, 96.

(5) Javaid, A.; Hughey, M. P.; Varutbangkul, V.; Ford, D. M. *J. Membr. Sci.* **2001**, *187*, 141.

(6) Honma, I.; Nomura, S.; Nakajima, H. *J. Membr. Sci.* **2001**, *185* (1), 83.

(7) Sudik, A. C.; Millward, A. R.; Ockwig, N. W.; Cote, A. P.; Kim, J.; Yaghi, O. M. *J. Am. Chem. Soc.* **2005**, *127*, 7110.

(8) Rowsell, J. L. C.; Millward, A. R.; Park, K. S.; Yaghi, O. M. *J. Am. Chem. Soc.* **2004**, *126*, 5666.

(9) Kitaura, R.; Kitagawa, S.; Kubtoa, Y.; Kobayashi, T. C.; Kindo, K.; Mita, Y.; Matsuo, A.; Kobayashi, M.; Chang, H.-C.; Ozawa, T. C.; Suzuki, M.; Sakata, M.; Takata, M. *Science* **2002**, *298*, 2358.

(10) Kitagawa, S.; Noro, S. *Compr. Coord. Chem. II* **2004**, *7*, 231.

(11) Yaghi, O. M.; O'Keeffe, M.; Ockwig, N. W.; Chae, H. K.; Eddaoudi, M.; Kim, J. *Nature* **2003**, *423*, 705.

(12) James, S. L. *Chem. Soc. Rev.* **2003**, *32*, 276.

(13) Rao, C. N. R.; Natarajan, S.; Vaidhyanathan, R. *Angew. Chem., Int. Ed.* **2005**, *43*, 1466.

(14) Kitagawa, S.; Kitaura, R.; Noro, S.-I. *Angew. Chem., Int. Ed.* **2004**, *43*, 2334.

(15) Papaefstathiou, G. S.; MacGillivray, L. R. *Coord. Chem. Rev.* **2003**, *246*, 169.

(16) Eddaoudi, M.; Moler, D. B.; Li, H.; Chen, B.; Reineke, T. M.; O'Keeffe, M.; Yaghi, O. M. *Acc. Chem. Res.* **2001**, *34*, 319.

(17) Finn, R. C.; Haushalter, R. C.; Zubieta, J. *Prog. Inorg. Chem.* **2003**, *51*, 421.

(18) Vioux, A.; LeBideau, J.; Mutin, P. H.; Leclercq, D. *Top. Curr. Chem.* **2004**, *232*, 145.

(19) Clearfield, A. *Curr. Opin. Solid State Mater. Sci.* **2003**, *6*, 495.

(20) Clearfield, A. *Prog. Inorg. Chem.* **1998**, *47*, 371.

10.1021/ic700790h CCC: $37.00

Scheme 1

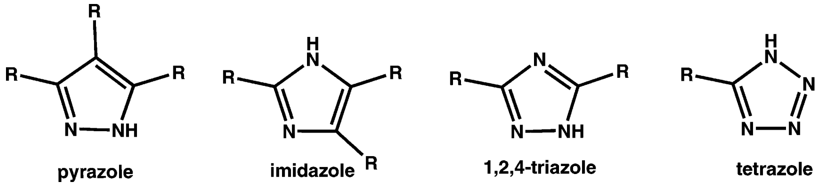

Scheme 2

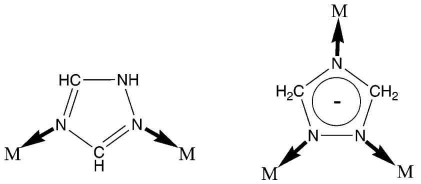

eroaromatic compounds such as pyrazole, imidazole, triazole, and tetrazole (Scheme 1) in their neutral and anionic forms have been exploited in the construction of complex organic−inorganic architectures.[23−26] Triazole, specifically, is an attractive ligand for the design of novel hybrid materials because of its ability to bridge multiple metal sites, a superexchange capacity reflected in unusual magnetic properties of its complexes, and its facile derivatization to provide bridging ligands with additional functionality.[27−34]

As a structural building block, triazolate may link metal centers through the N1 and N2 positions to provide one-dimensional and oligomeric secondary building units (Scheme 2). These building blocks can then be linked through the N4 positions to expand the dimensionality of the materials. In addition to the rich structural chemistry that evolves from such complex connectivity, transition-metal triazolates may exhibit interesting magnetic and optical properties. For example, magnetostructural correlations for copper(II) triazolates have been extensively reported.[32,35,36] Furthermore, the iron(II) triazolates exhibit spin-crossover characteristics and have potential applications as molecular devices.[37−40]

In an earlier study, we reported on the unusual magnetic properties of the copper(II) triazolate $[\{Cu_3(trz)_2\}V_4O_{12}]$.[41] Subsequently, the magnetostructural characteristics of a series of copper(II) triazolates and a cobalt(II) triazolate were reported by us.[42−44] Encouraged by these results, we investigated the hydrothermal syntheses, structures, and magnetic properties of a series of Mn^{II}, Fe^{II}, and Ni^{II} materials of the M^{II}/triazolate/anion family. The three-dimensional structures and magnetic properties of $[Mn_7(trz)_8(CH_3CO_2)_4(OH)_2]\cdot 2.5H_2O$ (**1**$\cdot 2.5H_2O$), $[Mn_5(Htrz)_2(SO_4)_4(OH)_2]$ (**2**), $[Fe_5(Htrz)_2(SO_4)_4(OH)_2]$ (**3**), $[Fe_3(Htrz)_3(HSO_4)(SO_4)_2(OH)]\cdot H_2O$ (**4**$\cdot H_2O$), $[Ni_3(trz)_3(OH)_3(H_2O)_4]\cdot 5H_2O$ (**5**$\cdot 5H_2O$), and $[Ni_3(trz)_5(OH)]\cdot 2.5H_2O$ (**6**$\cdot 2.5H_2O$) are reported.

Experimental Section

General Considerations. All chemicals were used as obtained without further purification. Iron(II) sulfate heptahydrate, ferrous ammonium sulfate hexahydrate, nickel(II) sulfate hexahydrate, manganese(II) sulfate monohydrate, nickel(II) oxide, manganese(II) 2,4-pentanedionate, ascorbic acid, 1,2,4-triazole, hydrofluoric acid (50%), and tetrabutylammonium hydroxide were purchased from Aldrich. All syntheses were carried out in 23 mL poly(tetrafluoroethylene)-lined stainless steel containers under autogenous pressure. The reactants were stirred briefly and the initial pH values measured before heating. H_2O was distilled above 3.0 MΩ in house using a Barnstead model 525 Biopure Distilled Water Center. The initial and final pH values of the reactions were measured using Hydrion pH sticks. The identities of the bulk materials for compounds **1**−**6** were established by comparing the observed powder X-ray diffraction (XRD) pattern to the calculated pattern from the single-crystal X-ray studies.

Synthesis of $[Mn_7(trz)_8(CH_3CO_2)_4(OH)_2]\cdot 2.5H_2O$ (1$\cdot$2.5H_2O). A solution of $Mn(CH_3CO_2)_2\cdot 4H_2O$ (1.980 g, 8.082 mmol), 1,2,4-triazole (0.181 g, 2.621 mmol), and H_2O (10.00 g, 556 mmol) with a mole ratio of 2.15:1.00:212 was stirred briefly before heating to 200 °C for 72 h (initial and final pH values of 7.0 and 6.5, respectively). Colorless blocks of **1**$\cdot 2.5H_2O$ were isolated in 75% yield (1.05 g). IR (KBr pellet, cm^{-1}): 3448(b), 1543(s), 1498(m), 1428(m), 1399(m), 1273(m), 1152(m), 1070(w), 1056(m), 1014(w), 991(m), 870(w), 670(m), 609(m). Anal. Calcd for $C_{24}H_{31}Mn_7N_{24}O_{10.5}$: C, 23.8; H, 2.57; N, 27.8. Found: C, 23.4; H,

---

(21) Alberti, G. In *Comprehensive Supramolecular Chemistry*; Atwood, J. L., Davis, J. E. D., Vogel, F., Eds.; Pergamon Press: New York, 1996; Vol. 9; Alberti, G., Bein, T., Eds.; pp 152−187.

(22) Ferey, G. *Chem. Mater.* **2001**, *13*, 3084.

(23) Beckmann, U.; Brooker, S. *Coord. Chem. Rev.* **2003**, *245*, 17.

(24) Haasnoot, J. G. *Coord. Chem. Rev.* **2000**, *200*, 131.

(25) Klingele, M. H.; Brooker, S. *Coord. Chem. Rev.* **2003**, *241*, 119.

(26) Zhang, J.-P.; Chen, X.-M. *Chem. Commun.* **2006**, 1689.

(27) Potts, K. T. *Chem. Rev.* **1961**, *61*, 87.

(28) Chivers, T.; Fu, Z.; Thompson, L. K. *Chem. Commun.* **2005**, 2339.

(29) Zhang, J.-P.; Lin, Y.-Y.; Huang, X.-C.; Chen, X.-M. *J. Am. Chem. Soc.* **2005**, *127*, 5495.

(30) Zhang, J.-P.; Zhang, S.-L.; Huang, X.-C.; Chen, X.-M. *Angew. Chem., Int. Ed.* **2004**, *43*, 206.

(31) Ferrer, S.; Lloret, F.; Bertomeu, I.; Alzuet, G.; Borras, J.; Garcia-Granda, S.; Liu-Gonzalez, M.; Haasnoot, J. G. *Inorg. Chem.* **2002**, *41*, 5821.

(32) Zhou, J.-H.; Cheng, R.-M.; Song, Y.; Li, Y.-Z.; Yu, Z.; Chen, X.-T.; Xue, Z.-L.; You, X.-Z. *Inorg. Chem.* **2005**, *44*, 8011 and references cited therein.

(33) Du, M.; Jiang, X.-J.; Zhao, X.-J. *Chem. Commun.* **2005**, 5521.

(34) Zhang, J.-P.; Lin, Y.-Y.; Zhang, W.-X.; Chen, X.-M. *J. Am. Chem. Soc.* **2005**, *127*, 14162.

(35) Klingele, M. H.; Boyd, P. D. W.; Moubaraki, B.; Murray, K. S.; Booker, S. *Eur. J. Inorg. Chem.* **2005**, 910.

(36) Ferrer, S.; van Korringsbruggen, P. J.; Haasnoot, J. G.; Reedijk, J.; Kooijman, H.; Spek, A. L.; Lezama, L.; Arif, A. M.; Miller, J. S. *J. Chem. Soc., Dalton Trans.* **1999**, 4269.

(37) Kahn, O.; Martinez, C. J. *Science* **1998**, *279*, 44 and references cited therein.

(38) Kröber, J.; Audiere, J. P.; Claude, R.; Codjovi, E.; Kahn, O.; Haasnoot, J. G.; Groliere, F.; Jay, C.; Bousseksou, A.; Linaies, J.; Varret, F.; Gonthier-Vassal, A. *Chem. Mater.* **1994**, *6*, 1404.

(39) Michalowitz, A.; Moscovici, J.; Ducourant, B.; Cracco, D.; Khan, O. *Chem. Mater.* **1995**, *7*, 1833.

(40) Verelst, M.; Sommier, C.; Lecaste, P.; Mosset, A.; Kahn, O. *Chem. Mater.* **1998**, *10*, 980.

(41) Hagrman, P. J.; Bridges, C.; Greedan, J. E.; Zubieta, J. *J. Chem. Soc., Dalton Trans.* **1999**, 2901.

(42) Ouellette, W.; Galan-Mascaros, J. R.; Dunbar, K. R.; Zubieta, J. *Inorg. Chem.* **2006**, *45*, 1909.

(43) Ouellette, W.; Yu, M. H.; O'Connor, C. J.; Hagrman, D.; Zubieta, J. *Angew. Chem., Int. Ed.* **2006**, *45*, 3497.

(44) Ouellette, W.; Prosvirin, A. V.; Chieffo, V.; Dunbar, K. R.; Hudson, B.; Zubieta, J. *Inorg. Chem.* **2006**, in press.

2.33; N, 27.3. The formulation **1**·$0.5H_2O$ ($C_{24}H_{31}Mn_7N_{24}O_{10.5}$) reflects the loss of two H_2O molecules of crystallization upon drying and standing for several days.

Synthesis of [$Mn_5(Htrz)_2(SO_4)_4(OH)_2$] (2). A solution of $MnSO_4·H_2O$ (1.185 g, 7.011 mmol), 1,2,4-triazole (0.183 g, 2.649 mmol), tetrabutylammonium hydroxide (0.200 mL, 0.308 mmol), and H_2O (10.00 g, 556 mmol) in a mole ratio of 2.65:1.00:210: 0.12 was stirred briefly before heating to 200 °C for 72 h (initial and final pH values were 7.0 and 6.5, respectively). Colorless blocks of **2**·$3H_2O$ suitable for XRD were isolated in 75% yield (0.87 g). IR (KBr pellet, cm^{-1}): 3551(m), 3284(s), 3102(m), 2998(w), 2968(w), 2907(w), 1528(w), 1508(m), 1488(m), 1399(m), 1303(w), 1226(m), 1212(m), 1139(s), 1097(s), 1033(m), 1000(m), 916(w), 792(m), 691(m), 631(s), 590(m), 444(m). Anal. Calcd for $C_4H_8Mn_5N_6O_{18}S_4$: C, 5.78; H, 0.96; N, 10.1. Found: C, 5.92; H, 0.76; N, 10.2.

Synthesis of [$Fe_5(Htrz)_2(SO_4)_4(OH)_2$] (3). A solution of $FeSO_4·7H_2O$ (0.459 g, 1.651 mmol), 1,2,4-triazole (0.230 g, 3.330 mmol), ascorbic acid (0.100 g, 0.568 mmol), and H_2O (10.00 g, 556 mmol) with a mole ratio of 0.50:1.00:0.17:167 was stirred briefly before heating to 200 °C for 48 h (initial and final pH values of 4.5 and 7.5, respectively). Yellow plates of **3** were isolated in 75% yield (0.21 g). IR (KBr pellet, cm^{-1}): 3534(m), 3277(m), 3102(m), 3002(w), 1817(w), 1637(w), 1492(m), 1405(m), 1283(w), 1214(m), 1154(s), 1103(s), 1040(m), 996(s), 833(m), 725(w), 629(m), 586(w), 469(w). Anal. Calcd for $C_4H_8Fe_5N_6O_{18}S_4$: C, 5.74; H, 0.96; N, 10.1. Found: C, 5.65; H, 1.03; N, 10.0.

Synthesis of [$Fe_3(Htrz)_3(HSO_4)(SO_4)_2(OH)$]·$H_2O$ (4·H_2O). A mixture of $FeSO_4NH_4·6H_2O$ (0.100 g, 0.255 mmol), 1,2,4-triazole (0.100 g, 1.448 mmol), ethanol (2.00 g, 43.41 mmol), ascorbic acid (0.015 g, 0.085 mmol), and H_2O (2.00 g, 111 mmol) in a mole ratio of 0.18:1.00:30.0:0.06:76.7 was stirred briefly before heating to 180 °C for 2 h. Initial and final pH values of 3.5 and 3.0, respectively, were recorded. Colorless blocks of **4** suitable for XRD were isolated in 90% yield (0.053 g). IR (KBr pellet, cm^{-1}): 3359(w), 3240(m), 3126(m), 3000(w), 2863(w), 1527(w), 1486(m), 1407(m), 1305(w), 1192(w), 1158(m), 1126(m), 1070(s), 1040(m), 902(w), 783(m), 623(s). Anal. Calcd for $C_6H_{13}Fe_3N_9O_7S_3$: C, 10.3; H, 1.86; N, 18.0. Found: C, 10.2; H, 1.66; N, 17.8.

Synthesis of [$Ni_3(trz)_3(OH)_3(H_2O)_4$]·$5H_2O$ (5·$5H_2O$). A solution of $NiSO_4·6H_2O$ (0.438 g, 1.666 mmol), 1,2,4-triazole (0.229 g, 3.315 mmol), HF (0.350 mL, 10.14 mmol), and H_2O (10.00 g, 556 mmol) in a mole ratio of 0.50:1.00:3.06:168 was stirred briefly before heating to 200 °C for 48 h (initial and final pH values were 1.5 and 1.5, respectively). Blue crystals of **5**·$5H_2O$ suitable for XRD were isolated in 90% yield (0.297 g). Upon standing, some water of crystallization is lost, and the sample used for single-crystal X-ray determination had the composition **5**·$5.5H_2O$. IR (KBr pellet, cm^{-1}): 3403(b), 1655(m), 1514(m), 1297(m), 1209(w), 1168(m), 1092(s), 1003(m), 979(w), 880(m), 672(m), 616(m). Anal. Calcd for $C_6H_{27}N_9Ni_3O_{12}$: C, 12.3; H, 4.59; N, 21.5. Found: C, 11.7; H, 4.62; N, 21.3.

Synthesis of [$Ni_3(trz)_5OH$]·$2.5H_2O$ (6·$2.5H_2O$). A solution of NiO (0.133 g, 1.781 mmol), 1,2,4-triazole (0.230 g, 3.330 mmol), HF (0.100 mL, 2.90 mmol), and H_2O (10.00 g, 556 mmol) in a mole ratio of 0.53:1.00:0.87:167 was stirred briefly before heating to 200 °C for 72 h (initial and final pH values of 3.0 and 3.0, respectively). Orange rods of **6**·$2.5H_2O$ were isolated in 20% yield (0.069 g). IR (KBr pellet, cm^{-1}): 3529(s), 3447(b), 3134(w0, 1655(w), 1508(m), 1397(m), 1341(m), 1280(m), 1160(m), 1078(w), 1033(m), 815(s), 675(w), 425(s). Anal. Calcd for $C_{10}H_{16}N_{15}Ni_3O_{3.5}$: C, 21.0; H, 2.80; N, 36.7. Found: C, 20.8; H, 2.75; N, 36.4.

X-ray Crystallography. Structural measurements were performed on a Bruker AXS SMART CCD diffactometer at low temperature (90 K) using graphite-monochromated Mo Kα radiation ($\lambda_{\text{Mo K}\alpha}$= 0.710 73 Å).[45] The data were corrected for Lorentz and polarization effects and absorption using *SADABS*.[46,47] The structures were solved by direct methods. All non-hydrogen atoms were refined anistropically. After all of the non-hydrogen atoms were located, the model was refined against F^2, initially using isotropic and later anistropic thermal displacement parameters. Hydrogen atoms were introduced in calculated positions and refined isotropically. Neutral atom scattering coefficients and anomalous dispersion corrections were taken from the *International Tables*, Vol. C. All calculations were performed using *SHELXTL* crystallographic software packages.[48]

Crystallographic details have been summarized in Table 1. Atomic positional parameters, full tables of bond lengths and angles, and anisotropic temperature factors are available in the Supporting Information in CIF format. Selected bond lengths and angles are given in Tables 2−6.

Vapor Adsorption Measurements. The water vapor adsorption measurements were obtained using a Micromeritics ASAP 2020 volumetric gas adsorption instrument equipped with a vapor dosing attachment. The crystalline sample of**5**·$5H_2O$ was evacuated under dynamic vacuum at 160 °C at a heating rate of 0.1 °C min^{-1} until the outgas rate was less than 2 mTorr min^{-1}. The warm and cold free-space correction measurements were taken using ultrahigh-purity helium gas. The water isotherm measurements at 298 K were measured in a constant-temperature bath using triple-distilled and degassed H_2O.

Results and Discussion

Syntheses and IR Spectroscopy. Hydrothermal reactions provide convenient routes for the isolation of kinetically stabilized phases of high purity in the form of single crystals.[49−58] Furthermore, the technique is readily adapted to the introduction of organic components in metal−ligand subunits in the design of organic/inorganic hybrid materials. Such phases are often typified by complex framework structures that lend themselves to applications in sorption, catalysis, and the design of magnetic, electroactive, and optical materials.

The compounds for this study were prepared under conventional hydrothermal conditions. Compounds **1**−**4**

---

(45) *SMART, Data Collection Software*, version 5.630; Bruker AXS Inc.: Madison, WI, 1997−2002.

(46) *SAINT Plus, Date Reduction Software*, version 6.45A; Bruker AXS Inc.: Madison, WI, 1997−2002.

(47) Sheldrick, G. M. *SADABS*; University of Göttingen: Göttingen, Germany, 1996.

(48) *SHELXTL PC*, version 6.12; Bruker AXS Inc.: Madison, WI, 2002.

(49) Stein, A.; Keller, S. W.; Mallouk, T. E. *Science* **1993**, *259*, 1558−1564.

(50) Laudise, R. A. *Chem. Eng. News* **1987**, Sept 28, 30−43.

(51) Gopalakrishnan, J. *Chem. Mater.* **1995**, *7*, 1265.

(52) Whittinghan, M. S. *Curr. Opin. Solid State Mater. Sci.* **1996**, *1*, 227.

(53) Weller, M.; Dann, S. E. *Curr. Opin. Solid State Mater. Sci.* **1998**, *3*, 137.

(54) Gopalakrishnan, J.; Bhuvanrh, N. S. P.; Rangan, K. K. *Curr. Opin. Solid State Mater. Sci.* **1996**, *1*, 285.

(55) Rabenau, A. *Angew. Chem., Int. Ed. Engl.* **1985**, *24*, 1026.

(56) Lobachev, A. N. *Crystallization processes under hydrothermal conditions*; Consultants Bureau: New York, 1973.

(57) (a) Yoshimura, M.; Suchanek, W. L.; Byrappa, K. *Mater. Res. Soc. Bull.* **2000**, Sept, 17. (b) Fing, S.; Xu, R. *Acc. Chem. Res.* **2001**, *34*, 239.

(58) Zubieta, J. Solid state methods, hydrothermal. *Compr. Coord. Chem. II* **2003**, *1*, 697.

Table 1. Summary of Crystallographic Data for the Structures of **1**$\cdot$2.5H_2O, **2**, **3**, **4**$\cdot H_2O$, **5**$\cdot$5H_2O, and **6**$\cdot$2.5H_2O

	1	**2**	**3**
empirical formula	$C_{12}H_{15.50}Mn_{3.50}N_{12}O_{5.25}$	$C_2H_4Mn_{2.50}N_3O_9S_2$	$C_2H_3Fe_{2.50}N_3O_9S_2$
fw	604.15	415.55	416.82
cryst syst	monoclinic	orthorhombic	orthorhombic
space group	*P*2(1)/*n*	*Pnma*	*Pnma*
a, Å	14.5500(6)	20.0097(9)	19.7957(10)
b, Å	9.2584(4)	14.6258(7)	14.3606(7)
c, Å	17.0287(7)	6.8073(3)	6.6990(3)
α, deg	90	90	90
β, deg	109.4280(10)	90	90
γ, deg	90	90	90
V, $Å^3$	2163.31(16)	1992.21(16)	1904.38(16)
Z	4	8	8
D_{calcd}, g cm^{-3}	1.855	2.771	2.908
μ, mm^{-1}	2.057	3.610	4.270
T, K	90	90	90
λ, Å	0.710 73	0.710 73	0.710 73
R1[a]	0.0268	0.0271	0.0384
wR2[b]	0.0726	0.0737	0.0996

	4	**5**	**6**
empirical formula	$C_3H_{6.50}Fe_{1.50}N_{4.50}O_7S_{1.50}$	$CH_{4.67}N_{1.50}Ni_{0.50}O_2$	$C_{1.25}H_2N_{1.88}Ni_{0.38}O_{0.44}$
fw	349.49	99.08	72.57
cryst syst	rhombohedral	cubic	orthorhombic
space group	*R*3*m*	$Fd\bar{3}c$	*Cmmm*
a, Å	14.2395(5)	25.2102(4)	7.1333(6)
b, Å	14.2395(5)	25.2102(4)	14.9011(12)
c, Å	8.5007(6)	25.2102(4)	9.0257(7)
α, deg	90	90	90
β, deg	90	90	90
γ, deg	120	90	90
V, $Å^3$	1492.71(13)	16022.5(4)	959.38(13)
Z	6	192	16
D_{calcd}, g cm^{-3}	2.333	1.972	2.101
μ, mm^{-1}	2.567	2.869	2.969
T, K	90	90	90
λ, Å	0.710 73	0.710 73	0.710 73
R1[a]	0.0342	0.0430	0.0358
wR2[b]	0.0802	0.1075	0.1059

[a] $R1 = \sum|F_o| - |F_c|/\sum|F_o|$. [b] $wR2 = \{\sum[w(F_o^2 - F_c^2)^2]/\sum[w(F_o^2)^2]^{1/2}\}$; $w = 1/[s^2(F_o^2) + (aP)^2 + bP]$; $P = [\max(F_o^2,0) + 2F_c^2]/3$.

Table 2. Selected Bond Lengths [Å] and Angles [deg] for **1**$\cdot$2.5H_2O[a]

Mn1−O1 (OH)	2.0988(12)	Mn3−N5	2.2043(13)
Mn1−O3	2.1227(12)	Mn3−N7	2.2185(14)
Mn1−N6#1	2.1878(13)	Mn3−O1 (OH)	2.2291(12)
Mn1−N1	2.2145(13)	Mn3−N2	2.2492(13)
Mn1−N11#2	2.2237(13)	Mn3−N12#5	2.3036(14)
Mn2−O4	2.1748(13)	Mn3−O5	2.3804(11)
Mn2−O2	2.1801(13)	Mn4−N8	2.1747(14)
Mn2−N4	2.2064(13)	Mn4−N8#5	2.1747(14)
Mn2−O1 (OH)	2.2243(11)	Mn4−O5	2.2255(11)
Mn2−N9#3	2.2322(14)	Mn4−O5#5	2.2255(11)
Mn2−N3#4	2.2504(13)	Mn4−N10	2.2403(13)
		Mn4−N10#5	2.2403(13)
O3−Mn1−N1	165.85(5)	N8−Mn4−N8#5	180.00(6)
O4−Mn2−O2	166.31(5)	O5−Mn4−O5#5	180.0
N4−Mn2−N9#3	169.25(5)	N10−Mn4−N10#5	180.0
O1−Mn2−N3#4	177.18(5)	Mn1−O1−Mn2	110.46(5)
N5−Mn3−N7	166.04(5)	Mn1−O1−Mn3	116.12(5)
O1−Mn3−N12#5	175.53(4)	Mn2−O1−Mn3	107.88(5)
N2−Mn3−O5	168.77(5)		

[a] Symmetry transformations used to generate equivalent atoms: #1, $-x + 1, -y, -z$; #2, $-x + 1/2, y - 1/2, -z + 1/2$; #3, $-x + 1/2, y + 1/2, -z + 1/2$; #4, $x, y + 1, z$; #5, $-x, -y, -z$; #6, $x, y - 1, z$.

exhibit incorporation of the anion of the inorganic salt starting materials into the final product. In contrast, the Ni^{II} phases, **5** and **6**, incorporate only hydroxide as the charge-balancing counterion. It is also noteworthy that all compounds of this study, **1**−**6**, incorporate hydroxide into the product.

The successful syntheses of these materials also required the introduction of a variety of reagents that do not appear in the product compositions but are necessary for isolation. Tetrabutylammonium hydroxide was added to the reaction mixture for **2** to achieve a neutral reaction pH. The preparations of **3** and **4** required ascorbic acid to prevent oxidation of the iron. In the syntheses of the Ni^{II} species **5** and **6**, HF was introduced to solubilize the reactants.

It has been observed that relatively minor changes in the hydrothermal reaction conditions can result in dramatically different structures. This feature of hydrothermal chemistry is illustrated by the structures and compositions of **3** and **4**$\cdot H_2O$, both of which were prepared from $FeSO_4\cdot 7H_2O$, 1,2,4-triazole, and ascorbic acid but at different stoichiometries and reaction pHs.

The IR spectra of the compounds are characterized by a medium-to-strong band in the 1480−1520 cm^{-1} range, associated with ν(C═N) of the triazole/triazolate. In addition, there is a great deal of structure in the 800−1400 cm^{-1} range associated with ligand vibrations. The phases that entrain the water of crystallization, **1**, **5**, and **6**, exhibit a strong, broad band at ca. 3400−3450 cm^{-1}, attributed to ν(O−H) of the H_2O. This feature is absent in the spectra of the other complexes.

Table 3. Selected Bond Lengths [Å] and Angles [deg] for **2** and **3**[a]

2		**3**	
Mn1−O1 (OH)	2.156(1)	Fe1−O1 (OH)	2.0986(15)
Mn1−O4#1	2.068(1)	Fe1−O3#9	2.028(2)
Mn1−O3#2	2.177(1)	Fe1−O4#10	2.129(2)
Mn1−O10#3	2.181(1)	Fe1−O8#10	2.1453(19)
Mn1−N2	2.248(1)	Fe1−N1	2.159(2)
Mn1−O2	2.334(1)	Fe1−O2	2.274(2)
Mn2−O1 (OH)	2.077(1)	Fe2−O1 (OH)	2.035(3)
Mn2−O6 (OH)	2.077(1)	Fe2−O6 (OH)	2.038(3)
Mn2−O2	2.202(1)	Fe2−O10#10	2.152(2)
Mn2−O2#4	2.202(1)	Fe2−O10#11	2.152(2)
Mn2−O9#3	2.205(1)	Fe2−O2	2.1526(19)
Mn2−O9#5	2.205(1)	Fe2−O2#12	2.1526(19)
Mn3−O7	2.072(1)	Fe3−O6 (OH)	2.0982(14)
Mn3−O6 (OH)	2.152(1)	Fe3−O9#13	2.038(2)
Mn3−O5	2.177(1)	Fe3−O5	2.1330(19)
Mn3−O8#6	2.191(1)	Fe3−O7	2.147(2)
Mn3−N3	2.262(1)	Fe3−N3	2.164(2)
Mn3−O9#3	2.326(1)	Fe3−O10#10	2.270(2)
O4#1−Mn1−O1	171.32(6)	O3#9−Fe1−O1	170.75(10)
O10#3−Mn1−N(2)	170.91(5)	O8#10−Fe1−N1	173.46(8)
O3#2−Mn1−O2	166.26(5)	O4#10−Fe1−O2	167.91(8)
O6−Mn2−O1	178.60(7)	O1−Fe2−O6	178.36(10)
O2#4−Mn2−O9#3	179.57(5)	O10#11−Fe2−O2	179.73(7)
O2−Mn2−O9#5	179.57(5)	O10#10−Fe2−O2#12	179.73(7)
O7−Mn3−O6	173.14(6)	O9#13−Fe3−O6	172.97(9)
O5−Mn3−N3	165.98(6)	O5−Fe3−N3	168.84(8)
O8#6−Mn3−O9#3	165.31(5)	O7−Fe3−O10#10	166.18(8)
Mn2−O1−Mn1	99.95(6)	Fe2−O1−Fe1	99.60(9)
Mn1−O1−Mn1#4	120.59(9)	Fe1#12−O1−Fe1	119.10(13)
Mn2−O2−Mn1	91.17(5)	Fe2−O6−Fe3	100.58(8)
Mn2−O6−Mn3	100.27(6)	Fe2−O2−Fe1	90.97(7)
Mn3#4−O6−Mn3	120.77(9)	Fe3#12−O6−Fe3	119.55(13)
Mn2#6−O9−Mn3#6	91.48(5)	Fe2#14−O10−Fe3#14	91.97(8)
S1−O2−Mn2	121.14(7)	S1−O2−Fe2	121.48(11)
S1−O2−Mn1	136.49(8)	S1−O2−Fe1	136.85(11)
S1−O3−Mn1#7	132.35(8)	S1−O3−Fe1#9	158.91(14)
S1−O4−Mn1#1	159.41(9)	S1−O4−Fe1#14	133.30(12)
S1−O5−Mn3	131.33(8)	S1−O5−Fe3	130.54(12)
S2−O7−Mn3	159.37(9)	S2−O7−Fe3	131.69(12)
S2−O8−Mn3#3	131.42(8)	S2−O8−Fe1#14	129.19(11)
S2−O9−Mn2#6	121.95(8)	S2−O9−Fe3#18	159.30(14)
S2−O9−Mn3#6	136.78(8)	S2−O10−Fe2#14	122.18(11)
S2−O10−Mn1#6	129.97(8)	S2−O10−Fe3#14	136.82(12)

[a] Symmetry transformations used to generate equivalent atoms for **2**: #1, $-x + 1, -y, -z + 1$; #2, $x, y, z - 1$; #3, $-x + {}^1/_2, -y, z - {}^1/_2$; #4, $x, -y + {}^1/_2, z$; #5, $-x + {}^1/_2, y + {}^1/_2, z - {}^1/_2$; #6, $-x + {}^1/_2, -y, z + {}^1/_2$; #7, $x, y, z + 1$. Symmetry transformations used to generate equivalent atoms for **3**: #9, $-x + 1, -y, -z + 2$; #10, $x, y, z + 1$; #11, $x, -y + {}^1/_2, z + 1$; #12, $x, -y + {}^1/_2, z$; #13, $-x + {}^1/_2, -y, z + {}^1/_2$; #14, $x, y, z - 1$; #18 $-x + {}^1/_2, -y, z - {}^1/_2$.

Table 4. Selected Bond Lengths [Å] and Angles [deg] for **4**·H_2O[a]

Fe1−O2	2.010(5)	Fe1−O3#2	2.164(3)
Fe1−O1 (OH)	2.0847(15)	Fe1−N1	2.177(3)
Fe1−O3#1	2.164(3)	Fe1−N1#3	2.177(3)
O2−Fe1−O1	172.7(4)	Fe1−O1−Fe1#5	116.41(11)
O3#2−Fe1−N1	169.49(17)	S1−O2−Fe1	158.4(7)
O3#1−Fe1−N1#3	169.49(17)	S1−O3−Fe1#6	138.8(2)
Fe1−O1−Fe1#4	116.41(11)		

[a] Symmetry transformations used to generate equivalent atoms: #1, $-y + {}^4/_3, -x + {}^5/_3, z - {}^1/_3$; #2, $-x + y + {}^4/_3, -x + {}^5/_3, z - {}^1/_3$; #3, $-x + y + 1, y, z$; #4, $-y + 2, x - y + 1, z$; #5, $-x + y + 1, -x + 2, z$; #6, $-y + {}^5/_3, x - y + {}^1/_3, z + {}^1/_3$; #7, $x, x - y + 1, z$.

Table 5. Selected Bond Lengths [Å] and Angles [deg] for **5**·$5H_2O$[a]

Ni1−O90#1	2.019(3)	Ni1−N1	2.035(3)
Ni1−O90	2.019(3)	Ni1−N1#1	2.035(3)
Ni1−N2#2	2.034(3)	Ni1−O1	2.0410(5)
O90#1−Ni1−O90	173.0(3)	N2#2−Ni1−O1	180.00(9)
N1−Ni1−N1#1	175.19(15)	Ni1−O1−Ni1#3	120.001(1)

[a] Symmetry transformations used to generate equivalent atoms: #1, $z + {}^1/_4, -y + 1, x - {}^1/_4$; #2, $-z + {}^1/_2, x + {}^1/_4, y - {}^1/_4$; #3, $-y + {}^3/_4, z + {}^1/_2, -x + {}^1/_4$; #4, $-z + {}^1/_4, -x + {}^3/_4, y - {}^1/_2$; #5, $-x + {}^1/_2, -z + {}^1/_2, -y + {}^1/_2$; #6, $y - {}^1/_4, z + {}^1/_4, -x + {}^1/_2$.

Table 6. Selected Bond Lengths [Å] and Angles [deg] for **6**·$2.5H_2O$[a]

Ni1−N1#1	2.000(3)	Ni2−N3	2.068(6)
Ni1−N1#2	2.000(3)	Ni2−N2	2.072(3)
Ni1−N1#3	2.000(3)	Ni2−N2#4	2.072(3)
Ni1−N1	2.000(3)	Ni2−N2#5	2.072(3)
Ni1−O90#1	2.110(13)	Ni2−N2#6	2.072(3)
Ni1−O90	2.110(13)	Ni2−O1#4	2.122(4)
Ni2−N3#4	2.068(6)	Ni2−O1	2.122(3)
N1#2−Ni1−N1#3	180.0(2)	N2−Ni2−N2#4	180.000(1)
O90#1−Ni1−O90	180.0	N2#5−Ni2−N2#6	180.00(12)
N3#4−Ni2−N3	179.999(2)		

[a] Symmetry transformations used to generate equivalent atoms: #1, $-x + 1, -y + 1, -z$; #2, $x, y, -z$; #3, $-x + 1, -y + 1, z$; #4, $-x + {}^3/_2, -y + {}^3/_2, -z + 1$; #5, $x, y, -z + 1$; #6, $-x + {}^3/_2, -y + {}^3/_2, z$; #7, $-x + 1, y, -z + 1$; #8, $-x + 1, y, z$; #9, $x, -y + 2, z$; #10, $-x + 1, -y + 2, -z + 1$; #11, $-x, -y + 1, -z$.

Description of the Structures. As shown in Figure 1, the structure of **1**·$2H_2O$ is constructed from heptanuclear Mn^{II} clusters linked through triazolate ligands into a three-dimensional framework. The heptanuclear manganese chain may be described as two μ^3-hydroxy-bridged triads linked through a central $\{MnN_4O_2\}$ site. Each triad consists of two manganese octahedra and one square pyramid. One of the octahedra of the triad exhibits $\{MnN_3O_3\}$ coordination geometry through bonding to three triazole nitrogen donors, the central μ^3-hydroxo group of the triad, and oxygen donors from two acetate ligands. The second octahedral site of the triad displays $\{MnN_4O_2\}$ coordination, bonding to four triazolate nitrogen donors, the μ_3-hydroxo group, and an acetate oxygen. The basal plane of the square-pyramidal site is defined by three triazolate nitrogen atoms and an acetate oxygen with the μ_3-hydroxo group in the apical position.

Each triad is associated with two acetate ligands and eight triazolate groups. One acetate bridges the square-pyramidal site to the chain-terminal octahedral manganese site, while the second bridges the two octahedral manganese centers of a triad and the inner octahedron of the triad to the central manganese site in the μ_3,η^2-coordination mode. Two of the triazolate ligands at the square-pyramidal site and two at the chain-terminal octahedral center of a triad bond through the N4 positions and direct the N1 and N2 donors toward neighboring heptanuclear chains. One triazolate bridges the square-pyramidal site and an octahedral site of a triad through the N1 and N2 nitrogen donors, directing the N4 position to a neighboring chain, while another heterocycle bridges the two octahedral sites of a triad and directs the N4 nitrogen donor to an adjacent chain. Two triazolate ligands bridge the inner octahedral manganese site of a triad to the central manganese octahedron. The central manganese of the heptanuclear chain enjoys $\{MnN_4O_2\}$ coordination defined by four triazolate nitrogen donors and two acetate oxygen donors. Thus, the corner-sharing arrangement of manganese

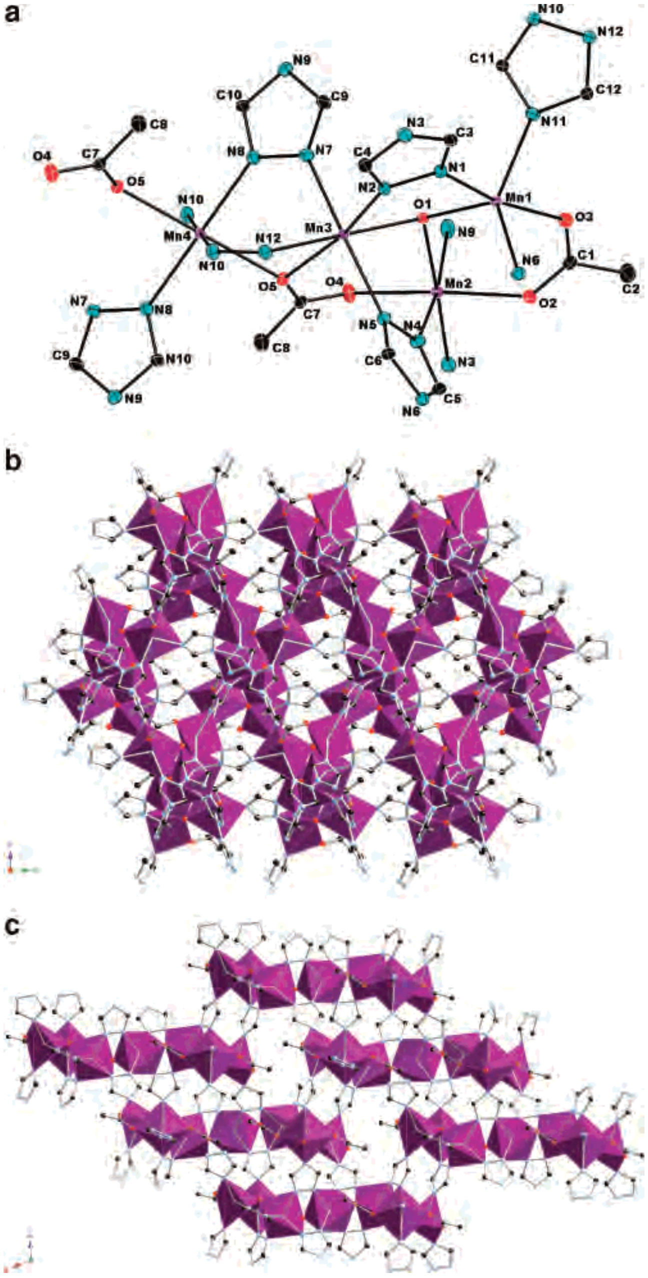

Figure 1. (a) ORTEP view of the structure of **1**·2.5H_2O, showing the atom-labeling scheme and 50% thermal ellipsoids. Note that Mn3 is actually six-coordinate through bonding to the N12 site of an adjacent manganese triad. (b) Polyhedral representation of the structure of **1** in the *bc* plane. (c) View of the structure of **1** in the *ac* plane, showing the linking of heptanuclear clusters in the plane. Atom-labeling scheme: oxygen, red spheres; carbon, black spheres; nitrogen, blue spheres; manganese, purple polyhedra.

polyhedra relies on μ^3-hydroxo and μ^2-acetate oxygen donors for connectivity.

Each cluster is associated with 16 triazolate ligands that link the cluster to four adjacent clusters in the *ac* plane and two additional chains in the *ab* plane to provide the three-dimensional connectivity. The H_2O molecules of crystallization occupy.

As shown in Figure 2, the structure of the sulfate phase **2** is also three-dimensional. The structure may be described as chains of Mn^{II} pentanuclear clusters linked through sulfate groups running parallel to the crystallographic *c* axis.

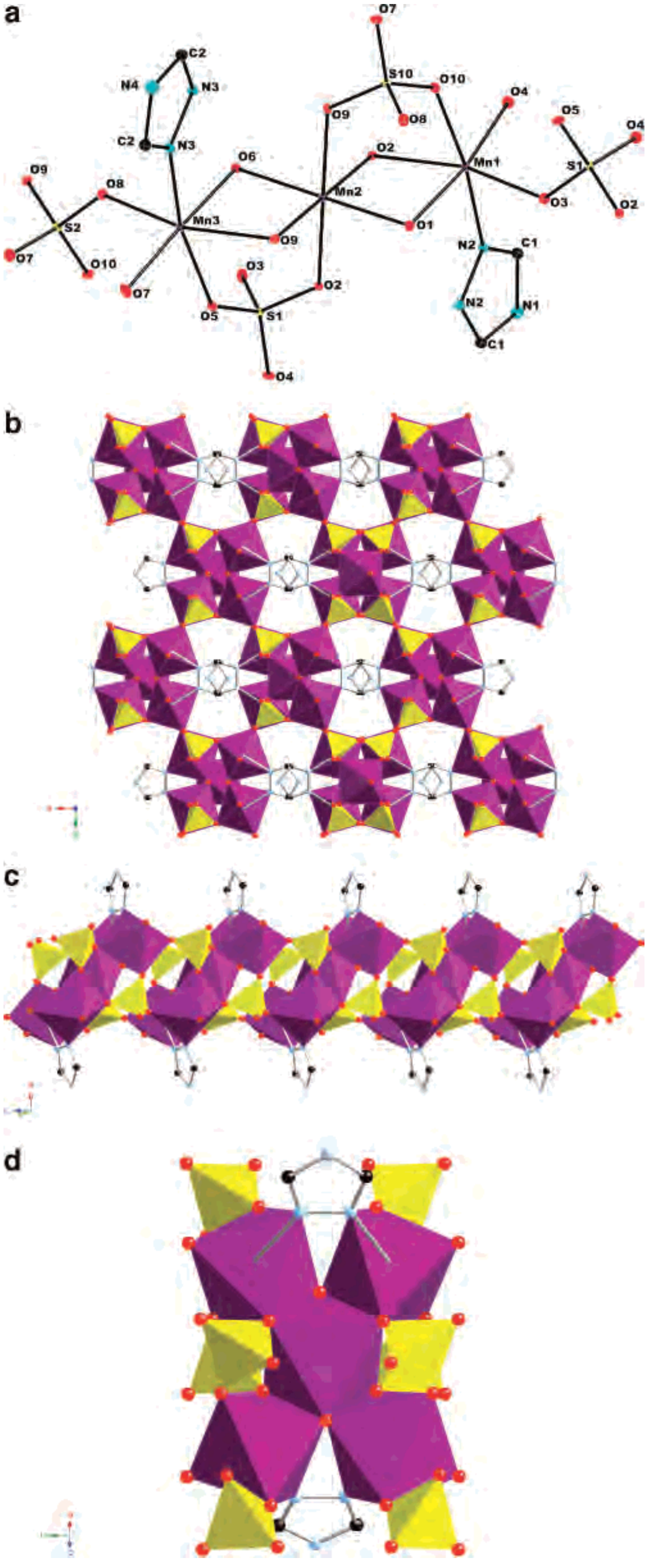

Figure 2. (a) ORTEP view of the structure of **2**, showing the atom-labeling scheme and 50% thermal ellipsoids. (b) Polyhedral representation of the structure of **2** in the *ab* plane. (c) View of the chain of sulfate-bridged clusters. (d) Pentanuclear substructure of **2**.

Adjacent chains are linked through sulfate tetrahedra. Each cluster consists of an aggregate of edge-sharing manganese octahedra, with the central manganese site sharing four edges with the peripheral sites. The {MnO_6} geometry of the central

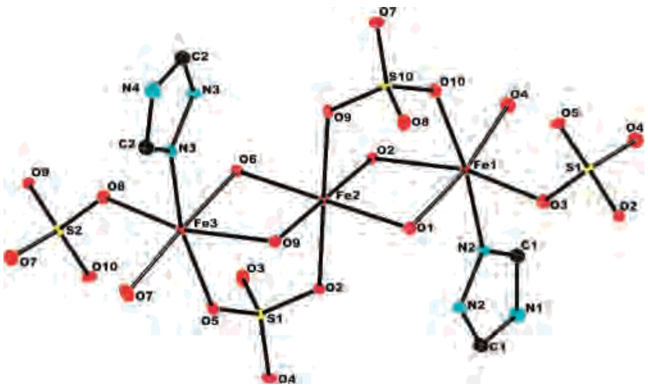

Figure 3. View of the atom-labeling scheme and 50% thermal ellipsoids for **3**.

manganese is defined by four sulfate oxygen donors and two μ^3-hydroxo groups in a trans orientation.

The peripheral manganese sites exhibit {MnO_5N} coordination geometry defined by four sulfate oxygen donors, the μ_3-hydroxo group, and a nitrogen donor from a neutral triazole ligand. Each cluster is associated with two Htrz ligands and 12 sulfate tetrahedra. The triazole groups each bridge two peripheral manganese octahedra through the N1 and N2 sites, leaving a protonated N4 site projecting into the channels running parallel to the *c* axis.

Four of the sulfate tetrahedra associated with a given cluster each use one vertex to bond the central manganese site and a peripheral site of the cluster in a μ_3 mode (Mn_2S) and a second vertex to bridge to a second manganese site. The third sulfate oxygen donor is used in bridging to an adjacent cluster of the chain with its axis parallel to the *c* axis (Figure 2). The final sulfate oxygen engages in bridging to an adjacent chain. Four additional sulfate tetrahedra each share a vertex with a peripheral manganese center of the cluster and direct two vertices to bridge to adjacent clusters of the chain. The fourth vertex is used to bridge to an adjacent chain. The final four sulfate groups share a vertex with each of the peripheral manganese sites of the cluster and use the remaining three oxygen donors to link to adjacent chains.

The structure of **3** (Figure 3) is isomorphous with that of **2**. As noted in Table 4, the bond-length differences between **2** and **3** reflect the contraction in the covalent radius of the metal in moving from left to right across the transition series. Thus, the average Mn−O(H) distance is 2.116(2) Å, while the average Fe−O(H) distance is 2.068(3) Å. Similarly, the average Mn−O(SO_4) and Mn−N distances are 2.195(2) and 2.255(2) Å, respectively, compared to an average Fe−O(SO_4) distance of 2.148(3) Å and an average Fe−N distance of 2.161(2) Å.

The three-dimensional structure of **4**·H_2O is shown in Figure 4. The secondary building unit of **4** consists of trinuclear clusters of Fe^{II} octahedra sharing a common vertex at a μ^3-hydroxo group. The trinuclear {$Fe_3(OH)(Htrz)_3$}$^{5+}$ core exhibits a bowl-shaped profile as a consequence of the cis disposition of the nitrogen donors from the bridging Htrz ligands at each iron site. The octahedral geometry at the metal centers is defined by N1 (N2) donors from two bridging Htrz ligands, the μ^3-hydroxo group, and oxygen donors from three sulfate groups.

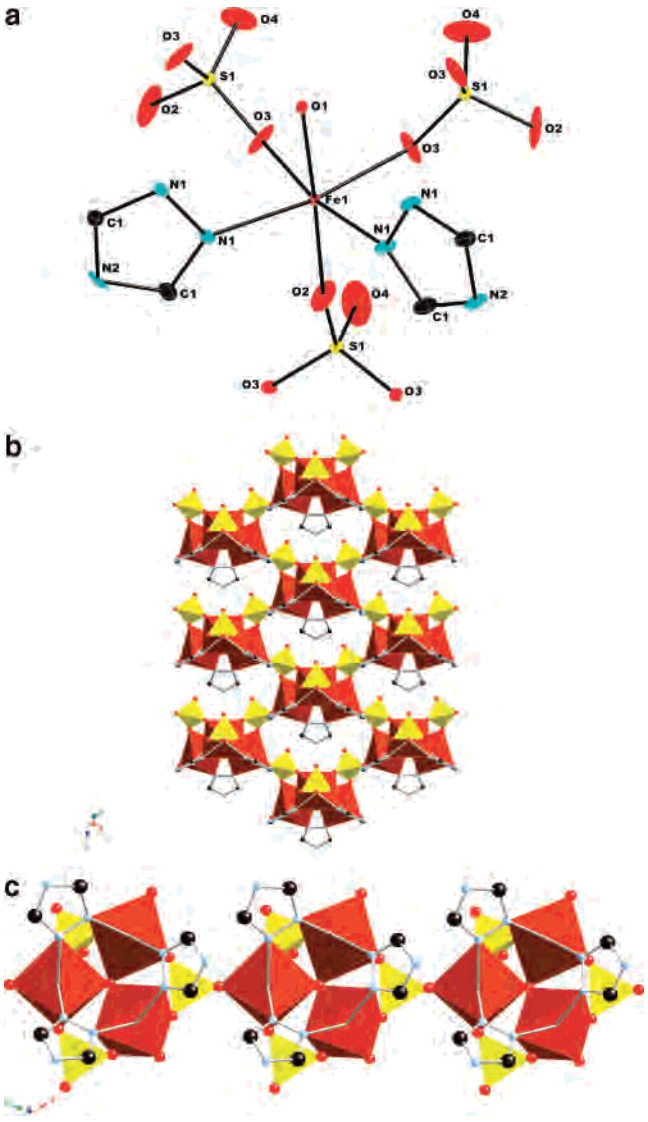

Figure 4. (a) Atom-labeling scheme and 50% thermal ellipsoids for **4**·H_2O. (b) Polyhedral representation of the three-dimensional structure of **4**. (c) View of the linking of the trinuclear building blocks of **4** through sulfate bridges to produce the one-dimensional substructure of **4**.

Each trinuclear subunit is associated with five sulfate ligands, three of which engage in O,O′-bridging within the cluster. One of these sulfate tetrahedra directs a third vertex to a neighboring cluster of a chain of trinuclear clusters that is disposed parallel to the *ab* plane. The fourth oxygen of this sulfate is pendant and projects into the cavity also occupied by the {NH} group of the Htrz ligand.

The remaining intracluster O,O′-bridging sulfate groups each direct an oxygen vertex to a cluster of a neighboring chain substructure, once again leaving a pendant {S═O} group on each sulfate group. Two iron sites of the triad each engage in vertex sharing with an additional sulfate group, linking the chain to two adjacent chains. Thus, each trinuclear cluster is associated with a total of six sulfate groups, two within the chain and four linking to adjacent chains.

The three-dimensional structure of**5**·5.5H_2O, shown in Figure 5, is also constructed from trinuclear secondary building units. The triangular {$Ni_3(\mu_3\text{-}OH)(trz)_3(OH)_2(H_2O)_4$} units exhibit Ni^{II} sites in “4 + 2” distorted octahedral

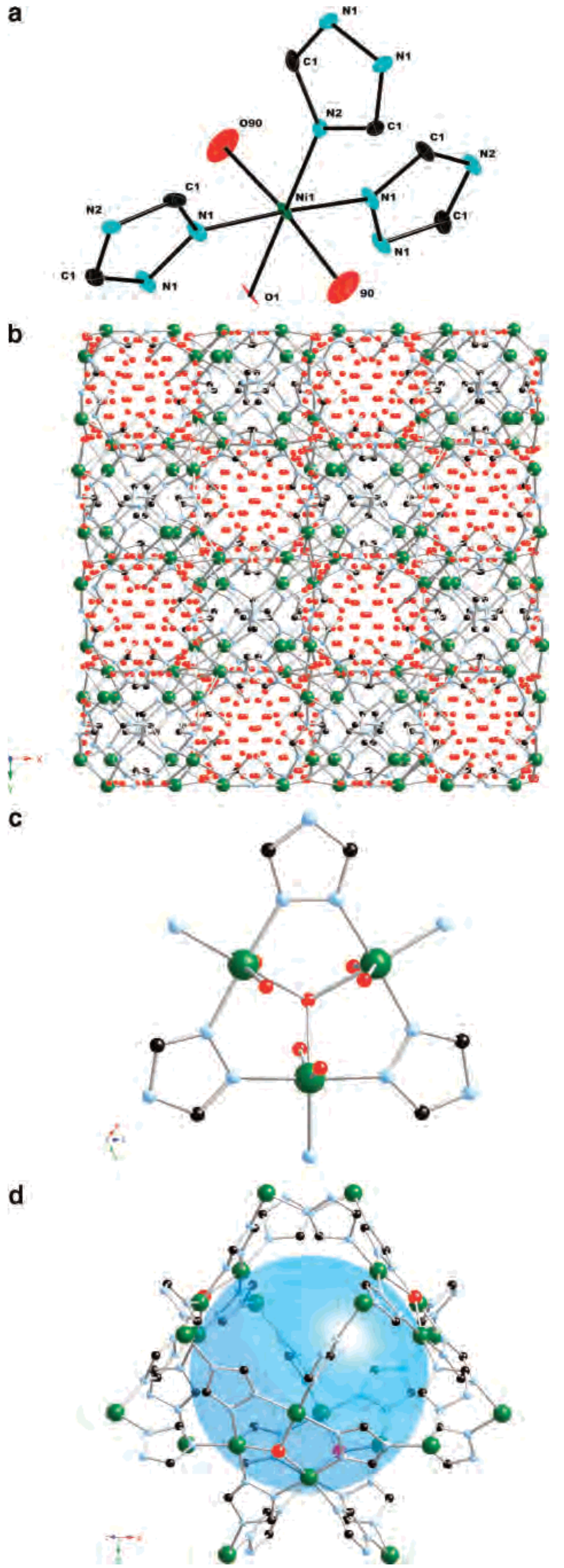

Figure 5. (a) ORTEP view of part of the structure of **5**$\cdot$5H_2O. (b) View of the three-dimensional structure of **5** in the *ab* plane. (c) Trinuclear secondary building unit of **5**. (d) View of the linking of secondary building units to produce a cavity of angstrom diameter.

geometry, defined by two nitrogen donors from trz ligands bridging nickel sites within the cluster through the N1 and N2 nitrogens, the μ_3-OH^- group, an N4 nitrogen atom from the trz ligand of an adjacent trinuclear cluster in the equatorial plane, and either two aqua ligands or an aqua ligand and an OH^- group occupying the axial positions. The N1 and N2 donors occupy trans sites on the metal, producing a $\{Ni_3N_6\}$ ring and a planar $\{Ni_3(trz)_3\}$ subunit, in contrast to the basket-shaped $\{Fe_3(Htrz)_3\}$ subunit of **4** (Figure 6). Each trinuclear building block is linked to six adjacent triangular subunits through six Ni−N4 interactions. The connectivity results in a three-dimensional metal−organic framework encompassing solvent-accessible channels of approximate diameter 12.45 Å, accounting for 47.1% of the unit cell volume.

The structure of **5** is isomorphous with that of the previously reported $[Cu_3(trz)_3(OH)_3(H_2O)_4]\cdot4.5H_2O$. The comparison of the bond lengths of the two analogues reveals the anticipated trend, with average Cu−O(H), $Cu-(OH)_2$, and Cu−N distances of 2.029(1), 2.070(5), and 1.983(2) Å, respectively, and average Ni−O(H), $Ni-OH_2$, and Ni−N distances of 2.0410(5), 2.019(3), and 2.035(3) Å, respectively. The lengthening of the axial $Cu-(OH)_2$ distance in comparison to that for $Ni-(OH)_2$ reflects the consequences of Jahn−Teller distortion of the Cu^{II} d^9 site, producing the common axial lengthening and “4 + 2” coordination geometry. The expansion of the coordination sphere of the Ni^{II} species relative to that of the Cu^{II} analogue is reflected in an increase of the cell volume of ca. 6% for compound **5** relative to $[Cu_3(trz)_3(OH)_3(H_2O)_4]$. This volume expansion is, in turn, related to the entrainment of ca. 20% more water of crystallization in **5** than in the Cu^{II} analogue.

As shown in Figure 7, the second nickel phase **6**$\cdot$2.5H_2O is also three-dimensional. The structure is constructed from $\{Ni_2(trz)_5(OH)\}_n^{2n-}$ chains (Figure 7b) linked through $\{Ni(H_2O)_2\}^{2+}$ units into a framework structure. The chain substructure exhibits $\{NiN_5O\}$ octahedra, defined by five N1 (N2) nitrogen donors and a μ^2-OH group. The Ni^{II} sites of the chain are alternately bridged by three N1 (N2) donors of three triazolate ligands and two N1 (N2) atoms and the μ_2-hydroxo group. The N4 position of each triazolate ligand bonds to the $\{Ni(H_2O)_2\}^{2+}$ site.

This second nickel site exhibits $\{NiN_4O_2\}$ octahedral coordination with an equatorial plane defined by four N4 nitrogen atoms from four triazolate ligands and two axial aqua ligands. Each of these nickel sites links four adjacent chains to generate the three-dimensional framework of **6**.

Table 7 summarizes some of the structural characteristics of metal complex materials with unsubstituted 1,2,4-triazole/triazolate. The table reveals a remarkably diverse structural chemistry, manifesting the absence of a persistent metal triazole or metal triazolate building block. The structural variability is a consequence of a number of determinants.

Unsubstituted 1,2,4-triazole may be present either as the neutral ligand Htrz, which may bridge two metal sites through either N1,N2 or N1,N4 coordination, or as the triazolate anion, which may bridge three metal centers through N1,N2,N4 coordination or two metal sites through the N1,N2-bridging mode. When the ligand is present as

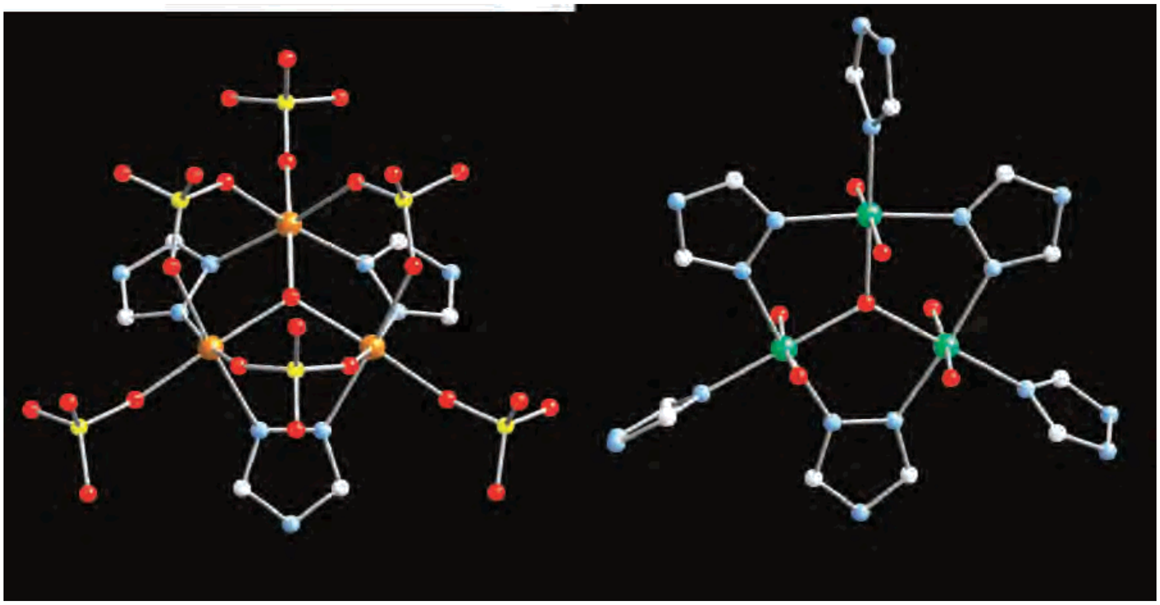

Figure 6. Trinuclear secondary building units of **4**$\cdot H_2O$ and **5**$\cdot 5H_2O$.

Htrz, the bidentate coordination mode restricts the spatial expansion of the metal/Htrz substructure. Thus, the structure $[M(NCS)_2(Htrz)]$ is one of only two examples of overall two-dimensional architectures for this family of materials. Similarly, $[M_5(Htrz)_2(SO_4)_4(OH)_2]$ and **4**$\cdot H_2O$ exhibit pentanuclear and trinuclear metal/Htrz building blocks, although the additional connectivity provided by the SO_4^{2-} groups produces overall three-dimensional structures.

When the anionic form 1,2,4-triazolate is present, the triply bridging mode is generally adopted, which correlates with cluster, chain, network, and framework metal/trz substructures. This diversity of structural subunits is a consequence of the coordination preferences of the metals, the presence of additional coordinating anions X^{n-}, and the interplay between these structural determinants. The requirements of the metal are most apparent in $[Co_2(trz)_3Cl]$, where the Co^{II} centers adopt both common coordination modes, octahedral and tetrahedral; the Cu^{II}-containing phases, which display the structural consequences of the Jahn−Teller distorted d^9 metal with "4 + 2", "4 + 1", and square-planar coordination sites; and the Cu^{I}-containing phases, which adopt tetrahedral, trigonal-planar, and linear coordination modes.

The structural possibilities are further enhanced by the presence of the auxiliary anion X^{n-} in the phases of the type M/trz/X^{n-} and M/Htrz/X^{n-}. These anionic components may be present as terminal ligands, as in $[M(NCS)_2(Htrz)]$, as monodentate bridges between two or three metal centers, as exemplified by $[Cu_2(trz)Cl_2]$, $[Zn(trz)Cl]$ and the hydroxide ligand in $[Zn_2(trz)(SO_4)(OH)]$, or as polyhedral components linking multiple metal sites, of which the sulfate phases $[M_5(Htrz)_2(SO_4)_4(OH)_2]$, **4**$\cdot H_2O$, and $[Cu_8(trz)_6(SO_4)_3(OH)_2(H_2O)]$ are representative. The interplay of the bridging Htrz or trz ligands and the bridging X^{n-} anions encourages spatial extension in multiple dimensions. Consequently, of 30 structures listed in the table, 26 are three-dimensional, while the remaining four are two-dimensional.

This bewildering array of architectures and substructures displayed by the materials of Table 7 is also made possible by the incorporation of aqua and hydroxide ligands, which can serve as terminal or bridging ligands. Furthermore, relatively minor variations in the hydrothermal reaction conditions can produce dramatically different structures, as noted for $[Fe_5(Htrz)_2(SO_4)(OH)_2]$ and **4**$\cdot H_2O$. In the case of the sulfate phases, the structures may be considered topologically metastable, in the sense that the structural variations arise from the promiscuous condensation of the metal polyhedra and the sulfate tetrahedron. This latter point is manifested in the soft M−O−S angles of the structures.

Thermal Properties. Compounds **1**−**5** of this study were analyzed by thermogravimetric analysis (TGA) under 20 mL min^{-1} of flowing nitrogen, while ramping the temperature at a rate of 5 °C min^{-1} from 25 to 800 °C. The thermal decomposition profile of **1**$\cdot 2.5H_2O$, as shown in Figure 8, exhibits a gradual weight loss of ca. 3.5% corresponding to the release of the water of crystallization (3.6% theoretical). The dehydration process is followed by a rapid weight decrease of 51% between 375 and 425 °C, corresponding to the loss of the triazolate groups and partial combustion of the acetate ligands. This behavior is similar to that of the M/triazolate/anion series for M = zinc and cadmium, which are also characterized by rapid weight losses in the 370−440 °C range associated with combustion of the triazolate ligands. The product of the thermal decomposition of **1** is a gray amorphous material.

As shown in Figure 9, the second manganese phase **2** also exhibits the characteristic rapid weight decrease between 410 and 440 °C, corresponding to the loss of the triazole ligands (17% observed; 16.6% theory). This process is followed by a gradual weight loss between 440 and 585 °C, followed by a second sharp step between 585 and 625 °C, related to the loss of SO_3 (41% observed; 38.3% theory). The product of the thermal decomposition of **2** is manganese oxide.

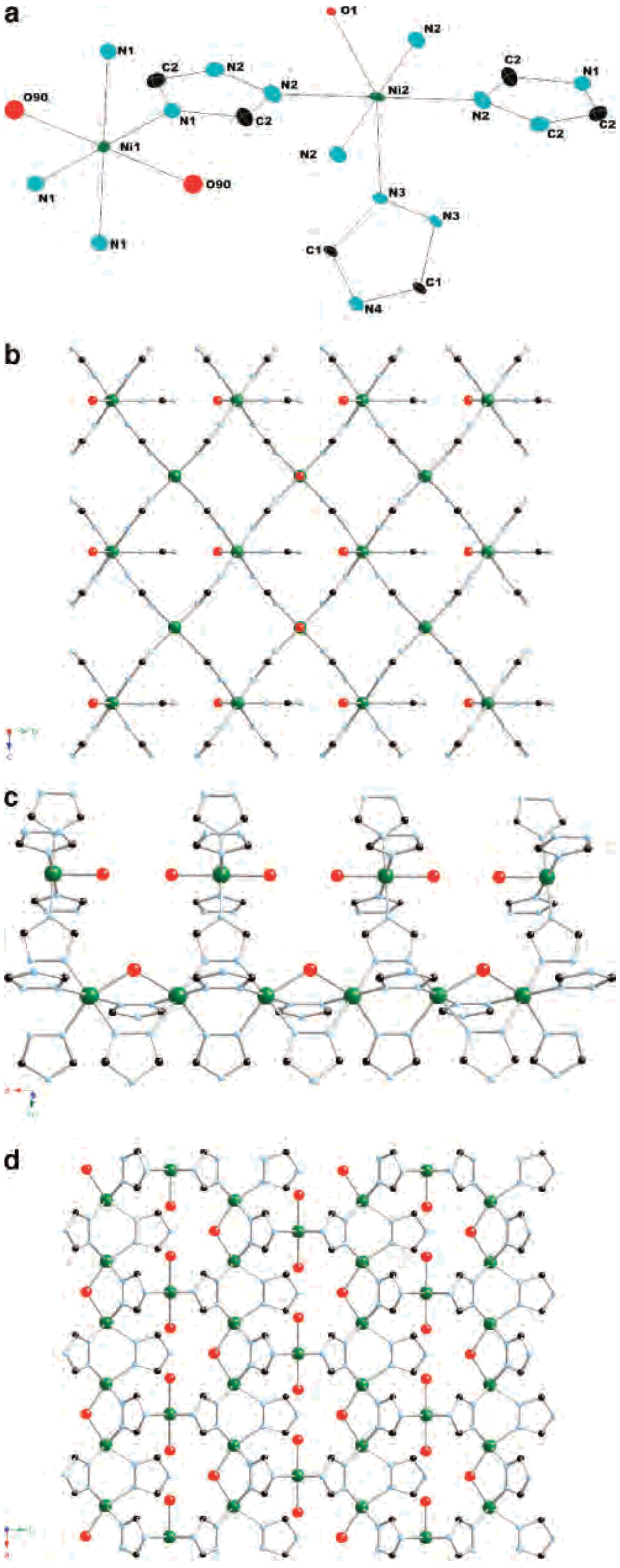

Figure 7. (a) Atom-labeling scheme and 50% thermal ellipsoids for the structure of **6**·2.5H_2O. (b) View of the three-dimensional structure of **6** in the *bc* plane. (c) $\{Ni_2(trz)_5(OH)\}_n{}^{2n-}$ chain substructure of **6**, showing the $\{Ni(H_2O)_2\}^{2+}$ subunits that connect adjacent chains. (d) Linking of $\{Ni_2(trz)_5(OH)\}_n{}^{2n-}$ chains by $\{Ni(H_2O)_2\}^{2+}$ units in the *ab* plane.

The isomorphous iron phase **3** exhibits a TGA profile similar to that of **2** (Supporting Information Figure S1) but with the initial and subsequent rapid weight losses occurring at lower temperatures: in the ranges 280−325 and 400−460 °C, respectively, in contrast to 410−440 and 585−625 °C, respectively, for **2**.

The thermal behavior of **4**·H_2O is characterized by a rapid decrease between 400 and 440 °C, corresponding to the loss of the triazole ligands and partial loss of SO_3 (Supporting Information Figure S2). The final gray amorphous product was not identified.

The TGA profile for **5**·5H_2O, as shown in Figure 10, indicates that the loss of water of crystallization commences just above room temperature, with subsequent rapid loss of H_2O between 140 and 190 °C (total weight loss from 25 to 190 °C, ca. 16%; 15.3% theoretical for 5H_2O). There is a plateau of stability from 190 to 430 °C, followed by a sharp decrease in weight between 460 and 480 °C of ca. 45% corresponding to the loss of the organic component and of the coordinated H_2O molecules (44.4% theoretical).

The thermodiffraction pattern for compound **5**·5H_2O in the temperature range 30−425 °C is shown in Figure 11. The X-ray profile of **5** undergoes a significant change as soon as the loss of water of crystallization commences at 75 °C. The dehydrated phase **5′** retains its structure well beyond the dehydration temperature to ca. 350 °C, whereupon the material begins to convert to an amorphous phase. While the structure of **5**·5H_2O changes upon dehydration to **5′**, this desolvated phase retains crystallinity. It is noteworthy that a sample of **5′**, prepared by heating under vacuum at 200 °C for 10 h, upon exposure to water vapor at room temperature will reabsorb solvent and revert to the original structure as monitored by XRD.

This observation suggests that the framework integrity of **5** is maintained after a desorption/absorption cycle and that **5′** may act as a sorbent of small guest molecules. To test this hypothesis, water vapor isotherms of **5′** were investigated. As shown in Figure 12, **5′** takes up considerable volumes of this gas, 12.1 wt % at 0.103 P/P_0 and 16.1% at 0.88 P/P_0. However, the material does not sorb methanol, O_2, N_2, or H_2. This observation most likely reflects the hydrophilicity of the void space and the tunnel topology, which is illustrated by the isosurface of Figure 13. The figure shows the interconnection of the large pores through intervening smaller channels of approximate diameter 4.0 Å and length 5.8 Å. It is also noteworthy that the coordinated H_2O molecules provide a highly polar void volume.

Magnetic Properties. Magnetic susceptibility measurements of complexes **2**−**6** were performed on polycrystalline samples of the compound at 1000 Oe over the temperature range 2−300 K. Some of the results are summarized in Table 8.

The value of χT at 300 K for **2** is 18.34 emu mol^{-1} K, which is lower than the expected value for five Mn^{II} ions, $S = {}^{5}/_{2}$ ($5\chi_{Mn}T = 21.875$ cm^3 mol^{-1} K; $g = 2.0$; Figure 14). The χT value continuously decreases from room temperature and reaches a minimum of 0.2 emu mol^{-1} K at 2 K. The temperature dependence of $1/\chi$ between 300 and 7 K approximates Curie−Weiss behavior with $C = 22.2$ emu mol^{-1} K and $\theta = -63$ K. The negative sign of the Curie−

Table 7. Summary of the Structural Characteristics of Materials of the M/trz, M/trz/anion, and M/Htrz/anion Families

compound	dimensionality	coordination geometry	structural features or substructures
$[M(NCS)_2(Htrz)]$	2D	octahedral, $\{MN_6\}$	N1,N4-bridging Htrz; two terminal NCS^- ligands at each metal site
1$\cdot 2.5H_2O$	3D	octahedral, $\{MnN_3O_3\}$ and $\{MnN_4O_2\}$; square pyramidal, $\{MnN_3O_2\}$	heptanuclear clusters
$[M_5(Htrz)_2(SO_4)_4(OH)_2]$ (M = Mn, Fe)	3D	octahedral, $\{MNO_5\}$ and $\{MO_6\}$	pentanuclear clusters
4$\cdot H_2O$	3D	octahedral, $\{FeN_2O_4\}$	trinuclear $\{Fe_3(\mu^3\text{-}OH)(Htrz)_3\}^{5+}$ clusters
$[M_3(trz)_3(OH)_3(H_2O)_4]\cdot xH_2O$	3D	octahedral, $\{MN_3O_3\}$	trinuclear $\{M_3(\mu^3\text{-}OH)(trz)_3\}^{2+}$ clusters
$[Ni_3(trz)_5(OH)]\cdot 2.5H_2O$	3D	octahedral, $\{NiN_5O\}$	chains with alternating triple bridges of three N1 (N2) triazolate donors, two N1 (N2) triazolate donors, and one hydroxide
$[Co_2(trz)_3Cl]$	3D	octahedral, $\{CoN_6\}$; tetrahedral, $\{CoN_3Cl\}$	chains of $\{CoN_6\}$ sites triply bridged by N1 (N2) triazolate donors
$[Cu_6(trz)_4Br_2]$	3D	linear, $\{CuN_2\}$; trigonal planar, $\{CuN_2I\}$	two-dimensional $\{Cu(trz)\}_n$ network
$[Cu_6(trz)_4Br][Cu_4Br_4OH]$	3D	diagonal, $\{CuN_2\}$ and $\{CuBr_2\}$	three-dimensional $\{Cu_6(trz)_4\}_n^{2n+}$ framework and one-dimensional $\{CuBr\}$ chain
$[Cu_3(trz)I_2]$	3D	linear, $\{CuN_2\}$; tetrahedral, $\{CuNI_3\}$ and $\{CuI_4\}$	$\{Cu(trz)\}_n$ and$\{CuI\}_n$ chains
$[Cu_4(trz)_3]OH$	3D	linear, $\{CuN_2\}$; trigonal planar, $\{CuN_3\}$	three-dimensional $\{Cu_4(trz)_3\}_n^{n+}$ framework
$[Cu_3(trz)_2][Cu_2(trz)Cl]Cl$	2D, 1D	Linear $\{CuN_2\}$ and $\{CuNCl\}$	$\{Cu_3(trz)_2\}_n^{n+}$ networks and $\{Cu_2(trz)Cl\}_n$ chains
$[Cu_3(trz)_4(H_2O)_3]F_2$	3D	square pyramidal, $\{CuN_4O\}$	$\{Cu_3(trz)(H_2O)\}_n^{2n+}$
$[Cu_2(trz)Cl_2]$	3D	octahedral, $\{CuN_2Cl_4\}$; trigonal planar, $\{CuNCl_2\}$	two-dimensional $\{Cu_2Cl_2\}_n^{n+}$ networks; triply bridged $\{CuN_2Cl_4\}$ sites through two chlorides and one N1 (N2) triazolate donor
$[Cu_2(trz)Br_2]$	3D	square pyramidal, $\{CuN_2Br_3\}$; trigonal planar, $(CuNBr_2\}$	$\{Cu(trz)Cl_2\}_n^{n-}$ chains
$[Cu_2(trz)_2][Cu_3I_4]$	3D, 1D	square planar, $\{CuN_4\}$; linear, $\{CuN_2\}$; trigonal planar, $\{CuI_3\}$	three-dimensional $\{Cu_2(trz)_2\}_n^{n+}$ framework with chains of $\{CuN_4\}$ sites doubly bridged by N1 (N2) triazolate donors; $\{Cu_3I_4\}_n^{n-}$ chains
$[Cu_8(trz)_6(SO_4)_3(OH)_2(H_2O)]$	3D	square planar, $\{CuN_2O_2\}$; square pyramidal, $\{CuN_3O_2\}$, $\{CuN_2O_3\}$; octahedral, $\{CuN_2O_4\}$; linear, $\{CuN_2\}$	two-dimensional $\{Cu_4(trz)_3(OH)\}_n^{2n+}$ networks with embedded $\{Cu_3(\mu^3\text{-}OH)(trz)_3\}^{2+}$ clusters
$[Cu_3(trz)_3(OH)][Cu_2Br_4]$	3D	octahedral, $\{CuN_3O_3\}$; tetrahedral, $\{CuBr_4\}$	three-dimensional $\{Cu_3(trz)_3(OH\}_n^{2n+}$ framework with embedded $\{Cu_3(\mu^3\text{-}OH)\ (trz)_3\}^{2+}$ clusters; three-dimensional $\{Cu_2Br_4\}_n^{2n-}$ framework
$[Zn(trz)_2]$	3D	tetrahedral, $\{ZnN_4\}$	$\{Zn_{10}(trz)_{12}\}$ cages
$[Zn(trz)F]\cdot 1.33H_2O$	3D	trigonal bipyramidal, $\{ZnF_2N_3\}$	$\{Zn(trz)F\}_n$ chains
$[Zn(trz)Cl]$	2D	tetrahedral, $\{ZnClN_3\}$	$\{Zn_2Cl_2(trz)_4\}^{2-}$ clusters and $\{Zn_4(trz)_4\}^{4+}$ rings
$[Zn(trz)Br]$	2D	tetrahedral, $\{ZnBrN_3\}$	$\{Zn_2Br_2(trz)_4\}^{2-}$ clusters and $\{Zn_4(trz)_4\}^{4+}$ rings
$[Zn_2(trz)_3(OH)]\cdot 3H_2O$	3D	$\{ZnON_3\}$	$\{Zn(trz)_3\}_n^{n-}$ chains
$[Zn_2(trz)(SO_4)(OH)]$	3D	octahedral, $\{ZnN_2O_4\}$	$\{Zn_3(\mu^3\text{-}OH)\}^{5+}$ clusters and $\{Zn_2(SO_4)(OH)\}_n^{n-}$ layers
$[Cd_3(trz)_3F_2(H_2O)]\cdot 2.75H_2O$	3D	octahedral, $\{CdN_3F_3\}$	$\{Cd_4F_4\}^{4+}$ clusters, $\{Cd_6(trz)_6F_4(H_2O)_2\}^{2+}$ clusters, and $\{Cd_6(trz)_6F_4(H_2O)_n^{2n+}$ chains
$[Cd_2(trz)_2Cl_2(H_2O)]$	3D	octahedral, $\{CdN_4Cl_2\}$ and $\{CdN_2Cl_3O\}$	$\{Cd(trz)_2Cl\}_n^{n-}$ and $\{Cd(trz)_2Cl_2(H_2O)\}_n^{2n-}$ chains
$[Cd_3(trz)_3Br_3]$	3D	octahedral, $\{CdN_2Br_4\}$ and $\{CdN_3Br_3\}$; trigonal bipyramidal, $\{CdN_4Br\}$	$\{Cd(trz)_2Br_2\}_n^{2n-}$ chains; $\{Cd_3(trz)_2Br_3\}_n^{n+}$ layers
$[Cd_2(trz)_3I]$	3D	octahedral, $\{CdN_6\}$, tetrahedral, $\{CdN_3O\}$	$\{Cd(trz)I\}$ chains
$[Cd_3(trz)_5(NO_3)(H_2O)]\cdot H_2O$	3D	octahedral, $\{CdN_6\}$; trigonal bipyramidal, $\{CdN_3O_2\}$ and $\{CdN_4O\}$	$\{Cd(trz)_3\}_n^{n-}$ chains; $\{Cd_2(trz)_7(H_2O)_2\}^{3-}$ clusters
$[Cd_8(trz)_4(OH)_2(SO_4)_5(H_2O)]$	3D	octahedral, $\{CdN_2O_4\}$, $\{CdNO_5\}$, and $\{CdO_6)$	$\{Cd_3(\mu^3\text{-}OH)\}^{5+}$ clusters, $\{Cd_7(trz)_4\}^{10n+}$ chains, and $\{Cd_8(SO_4)_5\}_n^{6n+}$ framework

Weiss constant and low room-temperature χT value indicate antiferromagnetic interactions between Mn^{II} centers. Below 7 K, a deviation from Curie−Weiss behavior due to single-ion anisotropy and short-range ordering is observed. No divergence between the zero-field-cooled (ZFC) and field-cooled (FC) data and no hysteresis loop were observed,

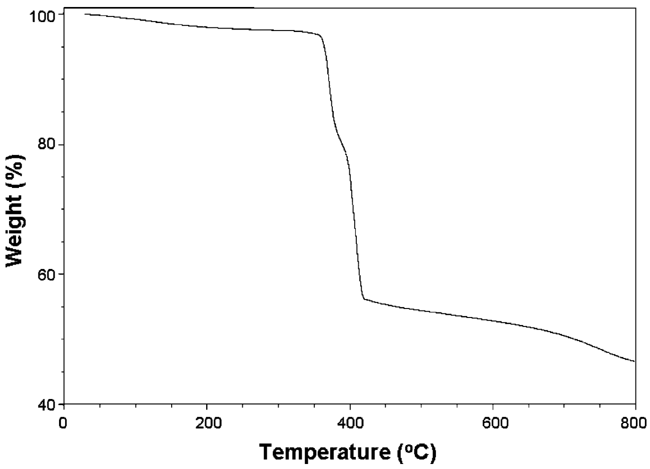

Figure 8. TGA profile for **1**·2.5H_2O in the 25−800 °C temperature range.

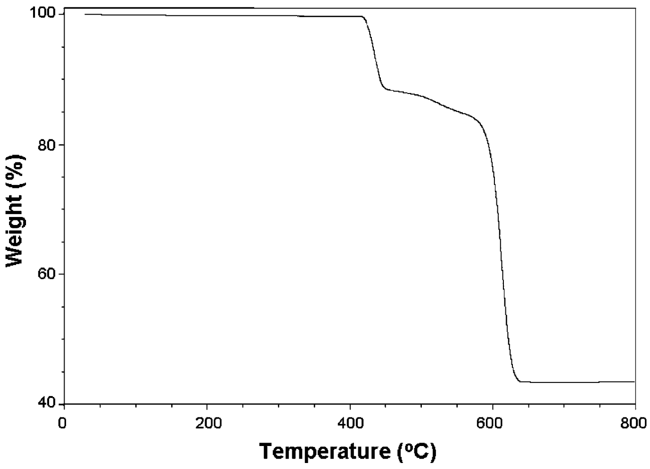

Figure 9. TGA profile for **2** in the 25−800 °C temperature range.

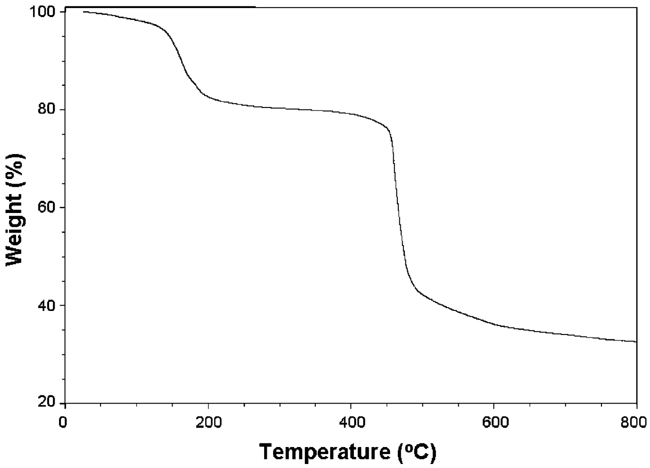

Figure 10. TGA profile for **5**·5H_2O in the 25−800 °C temperature range.

indicating unexceptional paramagnetic behavior. Consequently, even at 2 K, no long-range magnetic phase transition was observed, suggesting that $T_N < 2$ K. In frustrated systems like **2**, long-range magnetic ordering may be suppressed as a result of competing magnetic interactions.[59−62] The degree of spin frustration can be quantified by

$$f = |\theta|/T_N \tag{1}$$

A value of f between 1 and 10 is considered to be moderate frustration, higher than 10 as strong frustration. For compound **2**, the parameter $f > 30$ indicates very strong spin frustration.

In order to explain the magnetic interaction among different manganese ions, the local magnetic pathways and main magnetic repeat unit must be considered (Figure 15). The connectivity of the material dictates that bonding within the manganese pentamers formed by oxygen bridges will dominate the magnetic properties, with much weaker coupling between the pentamers through bridging triazolate groups.

To estimate the magnitude of the magnetic coupling between Mn^{II} centers, the temperature dependence of χT was modeled with MAGPACK[63] using the isotropic Heisenberg−Dirac−van Vleck Hamiltonian:

$$\mathscr{H} = -2J_1 \cdot S_1 \cdot (S_2 + S_3 + S_4 + S_5) - 2J_2 \cdot (S_2 + S_4) \cdot (S_3 + S_5) \tag{2}$$

where S_1 is the spin of the central manganese ion and J_1 is the isotropic magnetic exchange constant between the central and the rest of the Mn^{II} ions. Because of the large size of the resulting energy matrix and in order to avoid overparametrization, the exchange constant J_2 was assumed to be the same for all other Mn^{II} pairs of ions. The MAGPACK simulation resulted in the best-fit parameters $g_{Mn} = 2.0$, $J_1 = -2.2$ cm^{-1}, and $J_2 = -1.6$ cm^{-1}.

The value of χT at 300 K for **3** is 15.25 emu mol^{-1} K, which is again lower than the expected value for five independent Fe^{II} ions ($S = 2$), suggesting antiferromagnetic interactions (Figure 16). The χT value continuously decreases from room temperature and reaches a minimum of 0.26 emu mol^{-1} K at 2 K. The temperature dependence of $1/\chi$ between 300 and 30 K approximates Curie−Weiss behavior with $C = 17.8$ emu mol^{-1} K and $\theta = -50$ K. No long-range magnetic ordering below 30 K was observed. The degree of spin frustration is $f > 25$. The MAGPACK simulation of the χT vs T data was based on the Hamiltonian of eq 2 with S_1−S_5 corresponding to the Fe^{II} ions. The best agreement was achieved with the magnetic exchange constant $J_1 = J_2 = -2.3$ cm^{-1} and $g = 2.16$.

4·H_2O exhibits equilateral Fe^{II} triangles as the dominant magnetic repeat units. The value of χT at 300 K is 7.7 emu mol^{-1} K, which is smaller than the expected value for three Fe^{II} ions with $S = 2$ (Supporting Information Figure S3). The χT value continuously decreases from room temperature and reaches a minimum of 0.24 emu mol^{-1} K at 2 K. The temperature dependence of $1/\chi$ between 300 and 25 K

---

(59) Ramirez, A. P. *Annu. Rev. Mater. Sci.* **1994**, *24*, 453.

(60) Manson, J. L.; Ressouche, E.; Miller, J. S. *Inorg. Chem.* **2000**, *39*, 1135.

(61) Greedan, J. E. *J. Mater. Chem.* **2001**, *11*, 37.

(62) Zeng, M.-H.; Feng, X.-L.; Zhang, W.-X.; Chen, X.-M. *Dalton. Trans.* **2006**, 5294.

(63) Borrás-Almenar, J.; Clementa-Juan, J. M.; Coronado, E.; Tsukerblat, B. S. *J. Comput. Chem.* **2001**, *22*, 985.

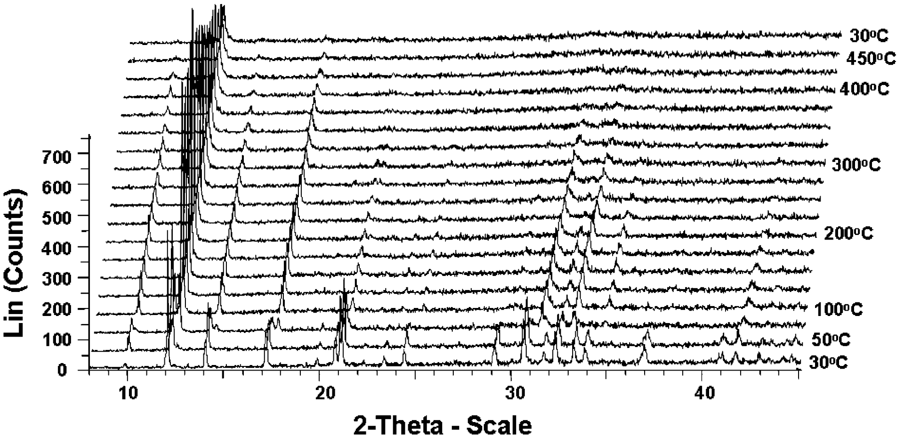

Figure 11. Thermodiffraction pattern for compound **5** in the 30−425 °C temperature range.

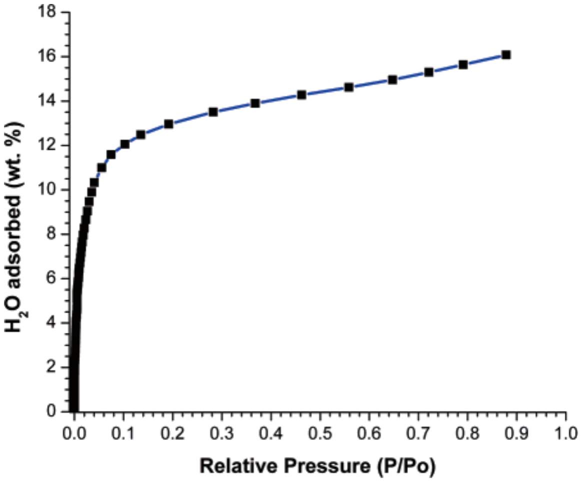

Figure 12. Water vapor isotherm for **5**.

approximates Curie−Weiss behavior with $C = 10.1$ emu mol^{-1} K and $\theta = -95$ K. No long-range magnetic ordering was observed. The degree of spin frustration is $f > 42$. The MAGPACK simulation of the χT vs T data was based on the simple triangular model with the Hamiltonian of eq 3:

$$\mathscr{H} = -2J\cdot(S_1\cdot S_2 + S_1\cdot S_3 + S_2\cdot S_3) \tag{3}$$

where S is the spin of the Fe^{II} ions and J is the isotropic magnetic exchange constant. The best agreement was achieved with the magnetic exchange constant $J = -5.9$ cm^{-1} and $g = 2.07$.

5$\cdot$5H$_2$O contains equilateral Ni^{II} triangles as the dominant magnetic repeat units. The value of χT at 300 K is 3.03 emu mol^{-1} K for compound **5**, which once again is smaller than the expected value for three Ni^{II} ions with $S = 1$ (Figure 17). The χT value continuously decreases from room temperature and reaches a minimum of 0.028 emu mol^{-1} K at 2 K. The temperature dependence of $1/\chi$ between 300 and 25 K approximates Curie−Weiss behavior with $C = 4.13$ emu mol^{-1} K and $\theta = -105$ K. Below 12 K, deviation from Curie−Weiss behavior is observed. The MAGPACK simulation of the χT vs T data was based on the Hamiltonian of eq 3, with S_1−S_3 corresponding to the Ni^{II} ions. Because of the magnetic interactions between the individual trimeric magnetic units, the simulated curve was corrected using the molecular field approximation (eq 4), where χ is the experimental exchange-coupled magnetic susceptibility, χ_{Ni} is the magnetic susceptibility of the Ni trimer, zJ' is the exchange parameter, and the other symbols have their usual meanings:[64]

$$\chi = \frac{\chi_{\mathrm{Ni}}}{1 - (zJ'/Ng^2\beta^2)\chi_{\mathrm{Ni}}} \tag{4}$$

The best agreement was achieved in the temperature range 12−300 K with the magnetic exchange constant $J = -10.0$ cm^{-1} and $g = 2.28$ and $zJ' = -10.5$ cm^{-1}. The application of different magnetic fields in the range of 50−1000 Oe showed a sharp maximum in χ between 7 and 5 K for compound **5**, with $\chi_{\max}$ moving slightly to higher temperatures with a strong increase in value (Figure 18). The shape of the sharp maxima in χ is indicative of long-range magnetic ordering. Evidence for the phase transition was confirmed by FC and ZFC measurements at 10 Oe. Results of the FC measurements exhibit two phase transitions at $T_{\mathrm{C1}} = 7$ K and $T_{\mathrm{C2}} = 5$ K, whereas ZFC exhibits only one transition at $T_{\mathrm{C}} = 7$ K (Figure 19). Above T_{C1} and below T_{C2}, the magnetization is reversible and behaves similarly for both FC and ZFC. Between T_{C1} and T_{C2}, however, there is nonreversibility, consistent with a spontaneous magnetization. Hysteresis loops measured at 6 K are consistent with a soft magnet for **5** with coercive fields of 110 Oe, and remnant (RM) magnetization values of 0.0005 μ_{B} (Figure 20). No hysteresis was observed below T_{C2}. Such behavior is reminiscent of reentrant ferromagnetism, which was first discovered in metal alloys in 1985[65] and subsequently found in other types of compounds.[66−69] The degree of spin frustration is calculated to be $f = |\theta|/T_{\mathrm{C1}} = 15$.

---

(64) Kahn, O. *Molecular Magnetism*; VCH: New York, 1993.

(65) Fujii, H.; Okamoto, T.; Shigeoka, T.; Iwata, N. *Solid State Commun.* **1985**, *53*, 715.

(66) Brabers, J. H. V. J.; Nolten, A. J.; Kayzel, F.; Lenczowski, S. H. J.; Buschow, K. H. J.; de Boer, F. R. *Phys. Rev. B* **1994**, *50*, 16410.

(67) Brinckerhoff, W. B.; Morin, B. G.; Brandon, E. J.; Miller, J. S.; Epstein, A. J. *J. Appl. Phys.* **1996**, *79*, 6147.

(68) Kim, W. S.; Chi, E. O.; Choi, H. S.; Hur, N. H.; Oh, S.-J.; Ri, H.-C. *Solid State Commun.* **2000**, *116*, 609.

(69) Buschmann, W. E.; Miller, J. S. *Inorg. Chem.* **2000**, *39*, 2411.

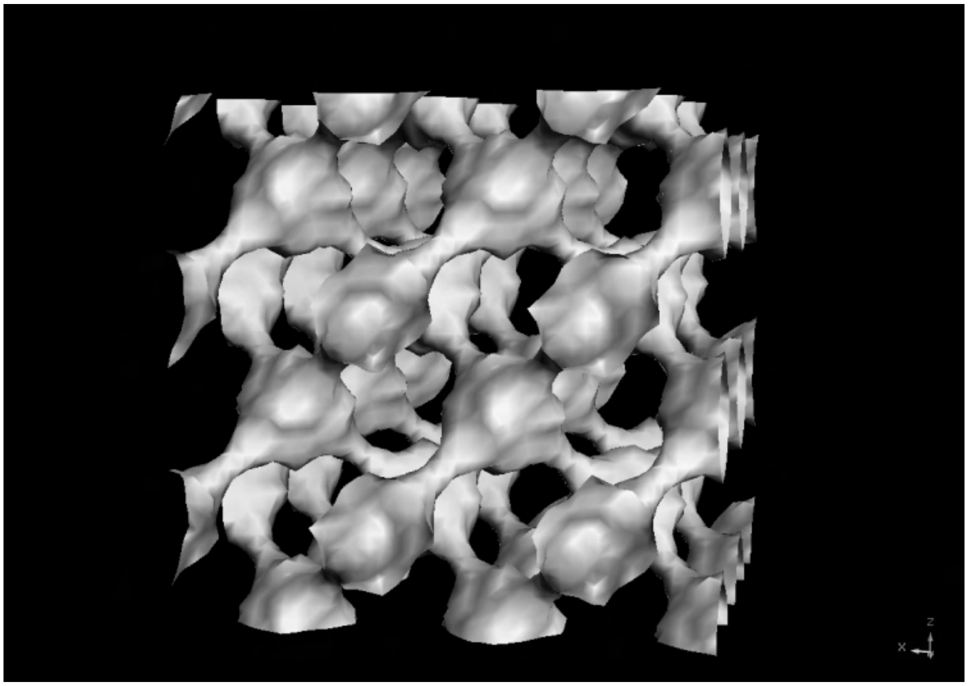

Figure 13. View of the isosurface (1.6 Å from the van der Waals radius) representing the tunnel structure of **5**.

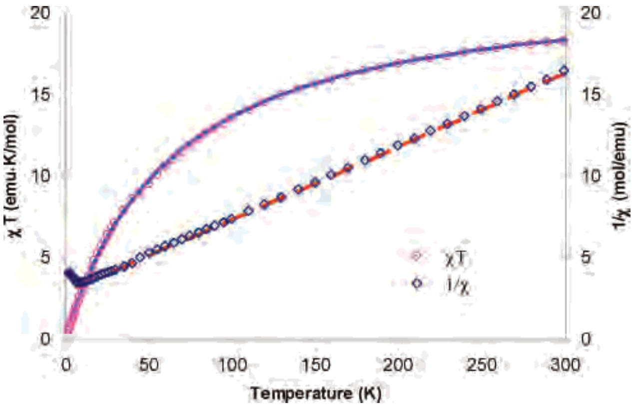

Figure 14. Temperature dependence of χT (○) and the inverse susceptibility (◇) for **2**. The solid line corresponds to the MAGPACK simulation using eq 2. The dashed line is the plot of the Curie−Weiss law.

Table 8. Summary of the Magnetic Properties of the Compounds **2**−**6**

compound	fitting model	J (cm^{-1})	zJ' (cm^{-1})	g	frustration degree f
2	pentamer	−2.2, −1.6	0	2.0	>30
3	pentamer	−2.3	0	2.16	>25
4	triangle	−5.9	0	2.07	>42
5	triangle	−10.0	−10.5	2.28	15
6	1D chain	−32.5	−0.5	2.32	

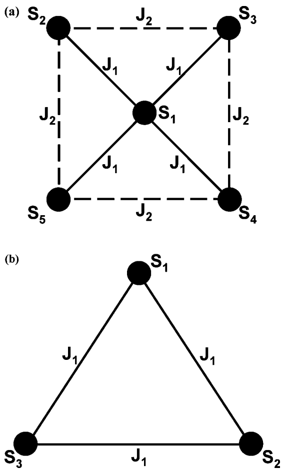

Figure 15. Schematic representations of the magnetic pathways (a) for the pentanuclear units of compounds **2** and **3** and (b) for the trinuclear units of compounds **4** and **5**.

The value of χT at 300 K for **6**·2.5H$_2$O is 3.06 emu mol^{-1} K, which is lower than the expected value for three Ni$^{\text{II}}$ ions with $S = 1$ (Supporting Information Figure S4). The χT value continuously decreases from room temperature and reaches a minimum of 0.16 emu mol^{-1} K at 2 K. The temperature dependence of $1/\chi$ between 300 and 40 K approximates Curie−Weiss behavior with $C = 4.13$ emu mol^{-1} K and $\theta = -105$ K. Compound **6** does not exhibit frustration, but rather it shows long-range magnetic ordering. The magnetic data were fit to the simple one-dimensional chain model[70] with the Hamiltonian $\mathcal{H} = -2J\cdot S_iS_{i-1}$. The parameters of the fitting are listed in Table 8. This model assumes that every third Ni$^{\text{II}}$ ion in the unit cell is isolated and its magnetism approximated with Curie−Weiss law with $C = 1.34$ emu mol^{-1} K and $\theta = -16$ K.

Conclusions

Conventional hydrothermal methods were used to prepare a series of materials of the general type M$^{\text{II}}$/triazole(olate)/anion where M$^{\text{II}}$ = Mn, Fe, and Ni. The diverse structural chemistry of these phases reflects several structural determinants, such as reaction conditions of stoichiometry, pH, and temperature, the identity of the anionic component, the

---

(70) Fisher, M. E. *Am. J. Phys.* **1964**, 32, 343.

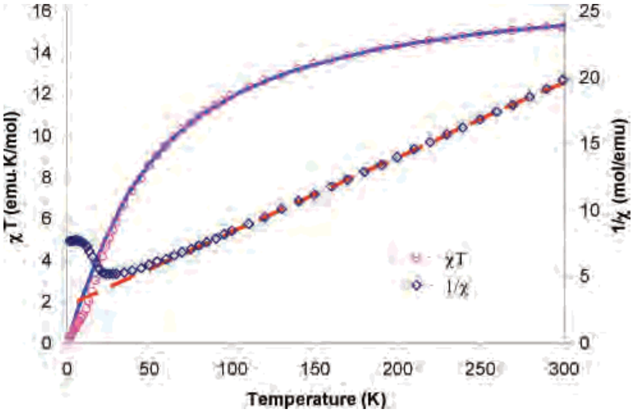

Figure 16. Temperature dependence of χT (○) and the inverse susceptibility (◇) for **3**. The solid line is the MAGPACK simulation using eq 2. The dashed line is the plot of the Curie−Weiss law.

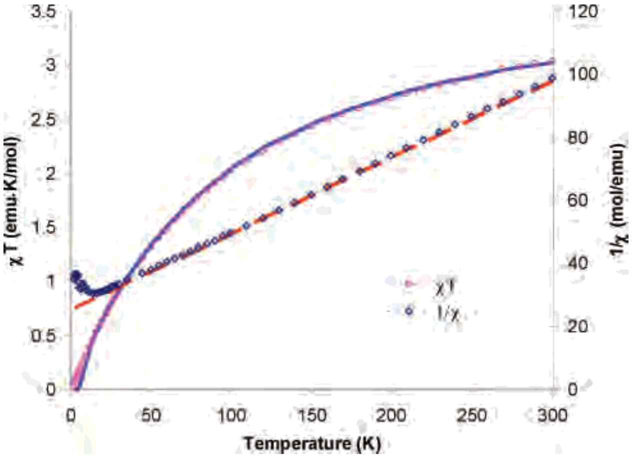

Figure 17. Temperature dependence of χT (○) and the inverse susceptibility (◇) for $\mathbf{5}\cdot 5H_2O$. The solid line is the MAGPACK simulation using eq 4. The dashed line is the plot of the Curie−Weiss law.

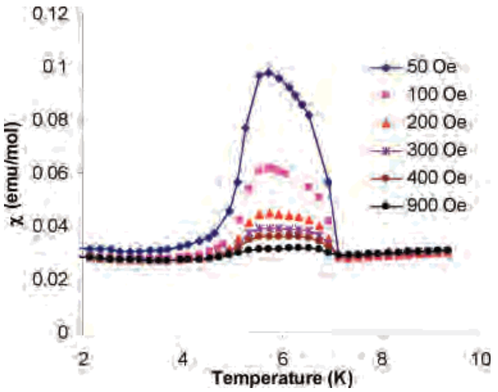

Figure 18. Temperature dependence of the direct current magnetic susceptibility for **5** at different applied magnetic fields.

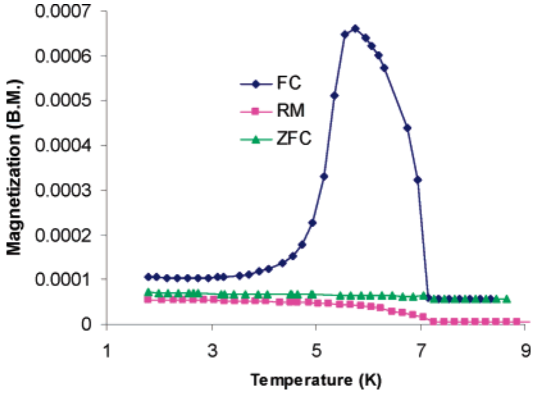

Figure 19. ZFC, FC, and RM magnetization data for **5** measured at applied field $H = 10$ Oe.

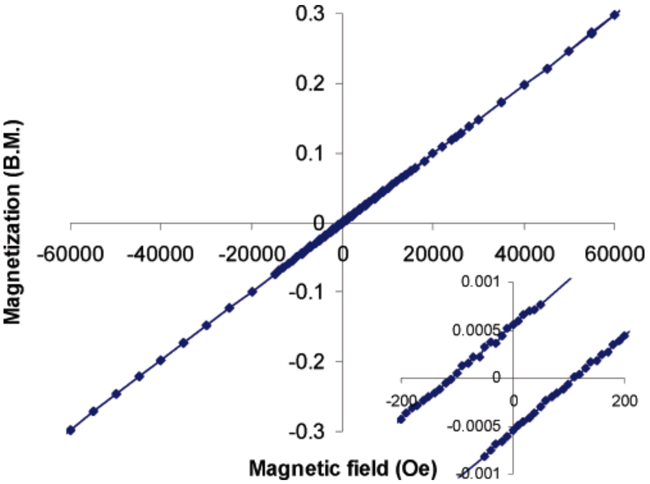

Figure 20. Hysteresis loop for **5** measured at 6 K.

coordination preferences of the transition-metal cation, and the di- and trinucleating properties of the neutral and anionic forms of triazole.

A recurrent theme of the structural chemistry of these materials is the presence of embedded transition-metal/triazole(olate) clusters as architectural motifs. Thus, compound **1** exhibits heptanuclear Mn^{II} building blocks. Similarly, compounds **2** and **3** manifest pentanuclear Mn^{II} and Fe^{II} clusters, respectively. While both **4** and **5** are characterized by trinuclear cluster moieties, the Fe^{II} clusters of **4** link to adjacent cluster sites through sulfate bridges exclusively as a consequence of the protonation of one nitrogen of the Htrz ligand, in contrast to the Ni^{II} clusters of **5**, which link directly to neighboring clusters through the triazolate ligands. Compound **6** is the only member of the series that is not constructed from cluster substructures but rather exhibits the chain structure $\{Ni_2(trz)_5(OH)\}_n^{2n-}$; chain motifs are common for Cu/trz and Fe/trz materials reported previously.[37,44]

As previously noted, variations in the hydrothermal reaction conditions can dramatically influence product compositions and structures of organic/inorganic materials. This observation is illustrated by the phases **3** and $\mathbf{4}\cdot H_2O$, which were prepared from the same starting materials at different pH values with different stoichiometries. Likewise, $\mathbf{5}\cdot 5H_2O$ and $\mathbf{6}\cdot 2.5H_2O$ were prepared under similar conditions but using $NiSO_4\cdot 6H_2O$ and NiO as the Ni^{II} source, respectively.

The large solvent-accessible volume associated with **5** suggested that the desolvated material **5′** might exhibit microporosity. The water vapor isotherms of **5′** did manifest classical type I behavior. However, methanol, N_2, O_2, and H_2 were not adsorbed by the material, presumably as a consequence of the narrow tunnels interconnecting the large pores of the void structure and the highly hydrophilic nature of the channels and pores.

The structural diversity of the materials of this study is reflected in their magnetic properties. The temperature-dependent magnetic susceptibilities of **2** and **3** are explained using the pentamer-fitting model, while those of **4** and **5** conform to the triangular-fitting model. Consequently, **2**−**5** exhibit varying degrees of spin frustration, with *f* in the range of 15 to >42.

The structural variety and unusual magnetism associated with these phases has encouraged us to pursue the development of materials of the M^{II}/triazole(olate)/anion family. We are currently investigating variations in the identity of the anion component, most notably by introducing phosphate and organophosphonate components.

Acknowledgment. This work was funded by a grant from the National Science Foundation (Grant CHE-0604527).

Supporting Information Available: Crystallographic files in CIF format for compounds **1**−**6**, Figures S1 and S2 showing the TGA profiles of **3** and **4**, respectively, and Figures S3 and S4 showing the temperature dependence of the magnetic susceptibility and the inverse susceptibility for **4** and **6**, respectively. This material is available free of charge via the Internet at http://pubs.acs.org.

IC700790H